Wishstone to Watchtower: Amorphous alteration of plagioclase-rich rocks in Gusev crater, Mars

Steven W. Ruff
School of Earth and Space Exploration, Arizona State University, Tempe, AZ 85287-6305, USA
steve.ruff@asu.edu

Victoria E. Hamilton
Southwest Research Institute, Boulder, CO 80302, USA
hamilton@boulder.swri.edu

Revision 2 submitted to

American Mineralogist

07/19/16

ABSTRACT

Previous observations by the Spirit rover in Gusev crater revealed a suite of rocks dubbed Wishstone and Watchtower Class in which the parent lithology and daughter products of a distinctive style of aqueous alteration are evident. Results from Spirit's Miniature Thermal Emission Spectrometer (Mini-TES; ~2000-340 cm^{-1}) were compromised by dust contamination of one of the instrument's mirrors, for which a correction has since been developed. Now we have documented nearly 200 examples of rocks encompassing the span of alteration from Wishstone Class, which spectrally resemble minimally altered plagioclase-phyric basalt, to the most altered Watchtower Class. Among them is a rock dubbed Bruce that may be a previously unrecognized alteration spectral end member. We employed factor analysis/target transformation and linear least squares modeling to investigate the spectral characteristics and mineralogy of these rocks. Our results amplify those of a prior preliminary analysis showing that alteration produced a material resembling basaltic glass that masks the spectral features of plagioclase. The association of this amorphous silicate component with a ferric iron nanophase oxide phase identified via Spirit's Mössbauer spectrometer is now clearly shown by our data, further characterizing the distinctive mineralogic expression of the alteration. These components and the absence of any recognizable secondary silicates or opaline silica may be an expression of alteration in the extreme aridity and cold of the Martian environment. Similar mineralogic characteristics of soil measured with the CheMin X-ray diffraction instrument on the Curiosity rover in Gale crater may be an indication that this alteration process is widespread on Mars.

Keywords: Mars, alteration, thermal infrared, spectroscopy, plagioclase, amorphous materials

INTRODUCTION

The Mars Exploration Rover Spirit encountered a remarkable diversity of rock types during its traverse of the Columbia Hills in Gusev crater, manifested both as variations in primary mineralogy and in secondary alteration (e.g., Arvidson et al. 2008). The classification of all rocks and soils observed by Spirit is based on elemental chemistry measured by the Alpha Particle X-ray Spectrometer (APXS), with subclasses defined where warranted by sufficiently large variations in Fe mineralogy measured by the Mössbauer spectrometer (MB) (e.g., Ming et al. 2006; Morris et al. 2006; Squyres et al. 2006). Both APXS and MB are contact instruments mounted on the rover's instrument deployment device (IDD) that allowed for interrogation of small (<3 cm) spots on rocks. Many of these spots were cleared of dust by the brush on the Rock Abrasion Tool (RAT), and in more limited cases, abraded by the RAT grind heads to expose fresh surfaces.

Wishstone and Watchtower Class were recognized as members of an alteration series identified by variations in geochemistry and Fe-bearing mineral phases (Hurowitz et al. 2006; Ming et al. 2006; Morris et al. 2006; Squyres et al. 2006). Work by Hurowitz et al. (2006) demonstrated a geochemical relationship consistent with two-component mixing between the less altered high Al_2O_3, TiO_2, CaO, Na_2O, P_2O_5 Wishstone Class end-member and an unidentified more altered end-member enriched in MgO, Zn, S, Br, and Cl. Watchtower Class is intermediate between these two end-members (Hurowitz et al. 2006). The alteration evident in the MB-derived Fe mineralogy is manifested as increasing values of nanophase ferric oxide (npOx), ferric to total iron ratio (Fe^{3+}/Fe_T), and mineralogical alteration index (MAI; the sum of npOx, hematite, goethite, and sulfate abundance) (Morris et al. 2008). The rocks of Watchtower

Class display sufficient variations among these parameters that it was subdivided into three subclasses in order of increasing alteration: Keystone, Keel, and Watchtower.

A preliminary assessment of the bulk mineralogy of these rock classes using thermal infrared (TIR) spectra from Spirit's Mini-TES revealed a dominant plagioclase component in Wishstone rock, and in Watchtower rock, up to 50% abundance of an amorphous component resembling basaltic glass (Ruff et al. 2006). These results were based on spectra from only a single rock for each class in part because most of the other examples were compromised by a sudden accumulation of dust on the Mini-TES elevation mirror on sol 420 of the mission, due to an aeolian event. Many tens of additional examples of Wishstone Class rocks were recognized following sol 420 despite the dust spectral artifacts, demonstrating it to be the most common rock type on the north side of Husband Hill (Ruff et al. 2006; Fig. 1). A robust correction for mirror-dust contamination has since been developed (Smith et al. 2006) and verified for surface observations (Ruff et al. 2011), allowing for more in-depth analyses of a suite of rocks that appears to record evidence for a particular style of Martian aqueous alteration.

Recent results from the Mars Science Laboratory rover Curiosity provide additional motivation for our study. Samples from an accumulation of drifted soil (a "sand shadow") called Rocknest measured by the Chemistry and Mineralogy (CheMin) X-ray diffraction (XRD) instrument on Curiosity contain as much as 45% by weight X-ray amorphous material along with mostly primary igneous crystalline phases including plagioclase, olivine, and pyroxene in order of decreasing abundance (Bish et al. 2013; Blake et al. 2013). The XRD pattern of the amorphous material in the Rocknest sand shadow can be fit with basaltic glass (Bish et al. 2013), but it likely represents a complex mixture including possible volcanic glass, hisingerite ($Fe_2Si_2O_5(OH)_4 \bullet 2(H_2O)$), amorphous S-bearing phases, and npOx (e.g., Dehouck et al. 2014;

McAdam et al. 2014; Sklute et al. 2015). The amorphous material also appears to be the host for 3 to 6 wt% H_2O (Leshin et al. 2013).

The Rocknest CheMin results add to a growing list of observations of poorly- or non-crystalline phases (hereafter referred to as amorphous) identified in Martian materials. Laboratory measurements of Martian meteorites, orbital remote sensing, and rover-based observations all have shown evidence for amorphous phases (e.g., Bandfield et al. 2000b; Glotch et al. 2006; Squyres et al. 2008; Changela and Bridges 2011; Horgan and Bell III 2012). Although the evidence is robust, in some cases it is not clear whether these phases are primary or secondary in origin, or perhaps indicative of phyllosilicates (Clark et al. 2007). The amorphous silica identified as opal-A in outcrops and soil adjacent to the Home Plate feature within a kilometer of Husband Hill, clearly resulted from hydrothermal activity in a volcanic setting (Squyres et al. 2008) and has retained its amorphous character without evidence for any transition to more crystalline forms (Ruff et al. 2011). So the origin and persistence of at least one example of an amorphous phase on Mars is well established. Wishstone and Watchtower Class rocks and their variants provide an opportunity to investigate in situ the nature of another example of an amorphous component on Mars.

DATA AND METHODS

Mini-TES instrument and spectra

Mini-TES spectra, which are the focus of this paper, provide information on the vibrational modes of molecular compounds. These modes are attributable to specific mineral phases in geologic materials. Details of the instrument design and operation are described by Christensen et al. (2003) and reviewed post-landing by Christensen et al. (2004) and Ruff et al. (2006). Briefly, Mini-TES is an interferometric spectrometer covering the range from ~2000 to 340 cm^{-1}

(~5–29 μm) with a spectral sampling of ~10 cm^{-1} and a nominal field of view (FOV) of 20 mrad. This FOV results in a spot size ~10 cm in diameter for targets (i.e., outcrops, rocks, and soils) nearest the rover, which increases with increasing distance to the target. As described by Ruff et al. (2006), the FOV is not sufficiently small to isolate the surfaces or interiors of rocks brushed or abraded by the Rock Abrasion Tool (RAT; Gorevan et al. (2003)). In the case of abraded surfaces (RAT holes), Mini-TES spectra include features attributable to scattering by fine particles that accumulate around the RAT hole from the grinding operation.

Each mirror-dust corrected Mini-TES spectrum presented in this paper is the average of 200 individual spectra constituting a single observation of a given target. Other dust-related spectral features are present in Mini-TES spectra that need to be described because of the variability they impart on otherwise similar spectra. As demonstrated by Ruff et al. (2006), Mini-TES spectra display certain features that are a function of the temperature difference between the target materials and the atmosphere. This behavior initially was thought to be due to atmospheric downwelling radiance contributing spectral features of atmospheric dust (Ruff et al. 2006). It was subsequently recognized that the contribution of optically thin surface dust likely was responsible, due to temperature differences between the dust and substrate material (Ruff and Bandfield 2010; Hamilton and Ruff 2012; Rivera-Hernandez et al. 2015). Spectral contributions of optically thin surface dust are most readily apparent from ~800 to ~1300 cm^{-1}, ranging from a reduction in contrast of the substrate spectrum to a complete inversion in apparent emissivity as the emitted radiance of the dust dominates (Fig. 2). Note that Figure 2 also shows that spectral features due to atmospheric CO_2 in the ~500 to ~800 cm^{-1} range tend to follow similar trends, because both effects are controlled by surface-atmosphere temperature differences.

Except where noted, the spectra shown in the current work have not been corrected for contributions from atmospheric CO_2, optically thin dust, or the more straightforward contributions of optically thick dust. Instead, the classification of rocks presented in subsequent sections relies on the low wavenumber range of Mini-TES spectra (<600 cm^{-1}), where dust in either form has much less impact (Ruff et al. 2006; Ruff et al. 2011; Hamilton and Ruff 2012) and atmospheric CO_2 features are minor. Dust lacks distinct spectral features in this range and has low opacity. An effort has been made to classify as many measured rocks and outcrops as possible, even those with substantial dust contributions. But in some cases, the spectral features of dust sufficiently obscure those of the substrate that classification is not possible. Some targets were measured more than once by Mini-TES. In those cases, the spectrum displaying the greatest contrast across both the ~800 to ~1300 cm^{-1} and <600 cm^{-1} ranges and least evidence for dust related artifacts is presented.

Determination of mineralogy

Linear least squares modeling. One of the approaches for identifying mineral components in the various spectral classes involves modeling using a linear least squares fitting algorithm and a library of reference spectra referred to as end-members (also known as linear deconvolution). This approach is based on the validated assumption that spectral contributions of individual components mix linearly, allowing each to be identified and their abundance (the areal fraction) to be determined (e.g., Thomson and Salisbury 1993; Ramsey and Christensen 1998; Feely and Christensen 1999; Hamilton and Christensen 2000). Note that this assumption generally applies to particulate mixtures with particle sizes greater than ~100 micrometers as well as mixed phase rocks independent of grain size.

We have experimented with two different linear least squares algorithms, those of Ramsey and Christensen (1998) and Rogers and Aharonson (2008). The former is a constrained least-squares linear retrieval (abbreviated here as CLS) that iteratively removes library spectra with negative coefficients until only those with positive values remain in the final solution. The latter version is a modification of a non-negative least squares (NNLS) algorithm. It retains all library spectra in the design matrix until the algorithm has converged on a best-fit solution, thus preventing the inadvertent ejection of a correct component early in the fitting process. Although NNLS model fits tend to have lower root-mean-square (RMS) residual error than those produced by the CLS algorithm, this typically requires more spectral end-members in the model solution with abundance levels that are insignificant (<1%; Rogers and Aharonson (2008)). Also noteworthy is the fact that in the case of one or more missing end-members from the spectral library, neither algorithm produces better results.

In the current work, we have applied the NNLS algorithm to model Mini-TES spectra. We do not report the results for modeled end-members that occur at <1% abundance given that they likely are unreliable components of the actual rocks. These modeled end-members are shown grouped as “other”, with their total number and abundance presented. End-members modeled with <10% abundance are presented but may or may not be robust identifications given the variable spectral contrast of various mineral phases and their resultant detectability. High spectral contrast phases are detectable in lower abundance, so may represent reliable detections at <10% abundance, which is considered a general detection limit (e.g., Feely and Christensen 1999). All modeled end-members and their mathematical uncertainty are shown rounded to the nearest integer. Various caveats regarding modeled mineralogy are included in the Results and Discussion sections.

Because we are interested in testing the previously identified chemical mixing trend in which Wishstone Class appears to be the least altered end-member (Hurowitz et al. 2006), we have included in the library an average Wishstone Class spectrum. Our work has identified a previously unrecognized candidate for an alteration spectral end-member, dubbed Bruce (see below), which we include in the library to assess the possible spectral mixing of the intermediate members of the Wishstone-Watchtower suite. In cases where either Wishstone or Bruce was part of a given model result, the algorithm was re-run without them to test the robustness of each as a true component, by quantifying the changes in RMS error, uncertainty value, and quality of spectral fit. This approach also allows us to assess the suite of mineral phases that fit the spectra independent of the two rock spectral end-members.

Following the approach of Ruff et al. (2006), the spectra were fit over the range ~380–1350 cm^{-1} (Mini-TES channels 5-102), which excludes the ends of the spectra where the signal-to-noise is low. The spectral range from ~560 – 780 cm^{-1} (channels 24 – 45) where atmospheric CO_2 is highly absorbing also was excluded. To account for spectral contributions from dust and thermal heterogeneity, three different dust variants and a “slope” spectrum were included in the end-member library (Ruff et al. 2006; Hamilton and Ruff 2012). A spectrum with unit emissivity (blackbody) also was used to address spectral contrast variations (e.g., Ramsey and Christensen 1998). These are shown among the “modeled” results versus the “normalized” results in which they have been subtracted and the remaining spectral components normalized. The full list of end-member spectra used for modeling is provided in Table 1.

Factor analysis and target transformation (FATT). We have applied the combination of factor analysis and target transformation (FATT) both to investigate the range of Mini-TES spectral classes and to recognize mineral components among the classes. This approach has been used successfully to separate compositional signatures in orbital Thermal Emission Spectrometer (TES) data (e.g., Bandfield et al. 2000b; Christensen et al. 2000; Glotch and Rogers 2013) and Mini-TES data acquired by the Opportunity rover in Meridiani Planum (Glotch and Bandfield 2006) and the Spirit rover in Gusev crater (Hamilton and Ruff 2012). It relies on two assumptions: (1) that there are independently varying components in the spectral data, such as atmospheric and/or surface components, and (2) that the components add linearly. In this study, we use the code and analytical approach described by Bandfield et al. (2000a) with details of the application to Mini-TES spectra described in Hamilton and Ruff (2012). Briefly, the factor analysis computes the eigenvectors and corresponding eigenvalues of the covariance matrix of the Mini-TES spectra. The number of eigenvectors, N, required to reconstruct these spectra to within the level of the noise of the data indicates how many linearly independent spectral components can be distinguished in the data set.

The eigenvectors are spectral in nature and may or may not resemble the spectra of geologic materials, but they do not have physical meaning. However, linear combinations of the eigenvectors can be used to reconstruct the spectral components present in a set of mixed data, even if the pure end members are not present. The eigenvalue associated with each eigenvector can be used to guide the selection of eigenvectors for this reconstruction. That is, a large drop in an eigenvalue below a given eigenvector indicates that subsequent eigenvectors with lower eigenvalues likely can be dismissed.

The eigenvectors are converted into physically meaningful spectra by applying a target transformation in which laboratory spectra (the ‘‘targets’’) are linearly fit using the N eigenvectors derived from the factor analysis (the subset of eigenvectors that excludes vectors attributable solely to noise) along with the mean and a blackbody (to account for contrast differences). Although laboratory spectra of real materials are used in this step, the eigenvectors are the spectral library used to fit them, not the other way around as is typical in other linear least squares models of thermal infrared data, such as the NNLS and CLS methods described above. If a known mineral or rock spectrum can be closely approximated by a linear combination of the eigenvectors, then that spectrum is a plausible component of the dataset. If the known spectrum is not a component of the dataset, the model shape produced from the eigenvectors will not fit it well, but the model shape will represent a valid component of the dataset (or a mixture of components). Spectral shapes that are recovered repeatedly, even if they do not match any of the target spectra, are reliable components of the data. Because spectral end-members often have greater contrast than mixed spectra, they typically recover the high contrast spectral end-members from the fitted eigenvectors, even when they do not produce a precise match. Additionally, unlike traditional linear least squares modeling of rock spectra, the target transformation task is not limited to positive values of the eigenvectors. Any linear combination of eigenvectors, including negative values, can be used to model the target spectra.

The Wishstone-Watchtower series represents a sequence of progressive alteration (Hurowitz et al. 2006; Ming et al. 2006; Morris et al. 2006; Squyres et al. 2006). We focused on using FATT to identify the dominant spectral components that might lead to compositional variability within the series and within subclasses, as described more fully in the next section. We performed factor analysis both on the entire series of Wishstone-Watchtower rocks (all subclasses, 193 spectra) as well as on individual subclasses. The resulting eigenvectors in both cases were used to model the mineral library, which is that used by Ruff et al. (2006) to model Wishstone spectra (Table 1). This target transformation step resulted in the recovery of spectral shapes that provide insight into the dominant sources of variability among the entire series, as well as within subclasses.

RESULTS: SPECTRAL CHARACTERISTICS AND DISTRIBUTION

Wishstone Subclass. Wishstone originally was recognized as a single class based on results from APXS and MB (Ming et al. 2008; Morris et al. 2008), but our work identifies the need to subdivide Mini-TES spectra of Wishstone Class rocks. The type example of the originally defined Wishstone Class occurs near the base of Husband Hill (Fig. 1) and was the subject of a measurement campaign using the full instrument suite starting on sol 333 (e.g., Arvidson et al. 2006). Two other examples that included measurements with the IDD instruments, called Wishing Well (target: Dreaming) and Champagne, occur within 10 meters. All three are float rocks. The last example of Wishstone Class material that included IDD measurements is a clast called Chic within the Bourgeoisie outcrop roughly midway up Husband Hill (Ming et al. 2008), a feature too small to isolate in a Mini-TES observation. No Wishstone subclasses were recognized among the four examples measured with APXS and MB. However, among the tens of Mini-TES spectra with Wishstone-like characteristics are variants of the type example in which the overall spectral similarity is preserved but some key departures are displayed repeatedly. We thus have defined Wishstone and M80 Subclasses.

The spectral characteristics of Wishstone Subclass were identified from the type example Wishstone, as well as Dreaming and adjacent rocks. Targeting of Mini-TES on the Wishstone Class rock Champagne was compromised by drift in the rover's inertial measurement unit (subsequently corrected), resulting in a spectrum of adjacent soil. As recognized by Ruff et al. (2006), the spectra of Wishstone rocks are dominated by features of plagioclase feldspar of intermediate An number (~An_{30} – An_{65}; Fig. 3). A relatively prominent peak at ~1080 cm^{-1} is a match to a comparable feature in plagioclase, but in some spectra is masked by a broad convex-upward feature between ~900-1200 cm^{-1} arising from optically thin surface dust. Features below 600 cm^{-1} tend to be the most diagnostic because this region of Mini-TES spectra is less affected by dust in any form (Ruff et al. 2006). Consequently, a set of features at ~560, 540, 490, and 455 cm^{-1} present in plagioclase and Wishstone Subclass serves as the most diagnostic for recognizing other examples (Fig. 3).

Wishstone Subclass spectra resemble that of a plagioclase-phyric basalt sample from Hole in the Ground maar in south central Oregon, USA (e.g., Heiken 1971) that likely represents basement rock related to the Cascade volcanic arc (Mariek Schmidt, personal communication)(Fig. 3). Sub-cm phenocrysts of plagioclase are the dominant phase of this rock and likewise produce its dominant spectral character in TIR data. Evidence for a greater proportion of olivine is manifested in the Wishstone Subclass spectrum as a relatively broad minimum at ~900 cm^{-1} and the reduced contrast of the low wavenumber plagioclase features compared with the Hole in the Ground spectrum. The spectral similarity between Wishstone Subclass and Hole in the Ground suggests a similar mineralogy, but not necessarily a similar volcanic process for their origin.

During the traverse of the north side of Husband Hill and the summit area named Hillary, and into the adjacent terrain known as Haskin Ridge (Fig. 1), Mini-TES observed 59 rocks with spectral characteristics consistent with the Wishstone type example (Fig. 4a and Appendix Table 1). No other examples of Wishstone Subclass beyond Haskin Ridge have been recognized. With the exception of the Chic clast, Wishstone Subclass was observed only as float rocks ranging from cobbles to small boulders, six of which are shown in Figure 5. An outcrop source has not been identified.

M80 Subclass. A rock named M80 measured by Mini-TES on sol 529, midway up Husband Hill, is the type example for a new subclass because it most clearly displays spectral features akin to Wishstone Subclass but with key distinguishing features that are found in tens of other examples. Although clearly retaining some of the spectral features of plagioclase, M80 departs from Wishstone Subclass with the appearance of a narrow, shallow minimum at ~510 cm^{-1} and the loss of Wishstone's emissivity maxima at ~490 and 455 cm^{-1} (Fig. 4b). The prominent emissivity minimum at ~540 cm^{-1} in Wishstone Subclass also is present in the M80 Subclass but is narrower and more symmetrical in M80. Finally, a weak peak near 900 cm^{-1} is present in many spectra of this subclass, although in some cases it is masked by the spectral distortions due to optically thin dust. Fifty-five rocks of the M80 Subclass were observed by Mini-TES from the base of Husband Hill on its north flank, through the summit region, and down onto Haskin Ridge (Appendix Table 2). Six examples are shown in Figure 5. No outcrop examples of M80 subclass have been recognized.

Watchtower Class

The type example of Watchtower Class is a rock that occurs immediately adjacent to an outcrop known as Larry's Lookout (Fig. 1) that shares similar Mini-TES spectral characteristics, clearly linking the two. Watchtower was the subject of a full IDD campaign beginning on sol 416. This was the last use of the grind capability of the RAT, during which the grind heads were abruptly worn down beyond their useable range, perhaps due in part to movement of the rock during the grind operation, as evidenced by small soil avalanches and displaced pebbles seen in post-grind images of the rock (Fig. 6). The movements indicate that Watchtower is either loosened outcrop or a displaced float rock.

Eleven examples of Watchtower Class were measured with the IDD instruments (Hurowitz et al. 2006; Ming et al. 2008). Although their chemistry allows all eleven to be grouped into a single class, results from MB show systematic variations in npOx, Fe^{3+}/Fe_T, and MAI sufficient to define three subclasses (Morris et al. 2006; Morris et al. 2008). The least altered is Keystone Subclass, followed by Keel Subclass, and the most altered Watchtower Subclass, each of which is presented below.

Keystone Subclass. Keystone Subclass is recognized as the least altered of the three previously defined Watchtower subclasses (Morris et al. 2008). Only two targets of the Keystone Subclass were measured with the IDD instruments, both on the outcrop known as Methuselah immediately west of the larger Jibsheet Ridge outcrop (Fig. 1). The surface texture of the Methuselah outcrop is notably rough, with sub-cm scale pits and protuberances that in the case of the Keystone target, look vaguely aligned. These give the appearance of fine-scale laminations (Squyres et al. 2006), although they are not manifested elsewhere on the outcrop. This texture creates voids that trap soil and dust, yielding Mini-TES spectra that in some cases do not display recognizable features of the underlying rock.

The Keystone IDD target was so dusty that the Mini-TES spectrum is dominated by features attributable to dust. A second Mini-TES target known as Madam, lower down on the same portion of the Methuselah outcrop within 10 cm of the Keystone target, was somewhat cleaner and provides a better spectrum to guide our analysis. A sharp inflection point at ~540 cm^{-1} is the sole manifestation of a plagioclase feature, with an unusually flat portion extending to lower wavenumbers (Fig. 4c). This combination of characteristics was used to classify other examples of Keystone Subclass.

Thirteen examples of Keystone Subclass were observed, dominated by targets on the Methuselah outcrop and five float rocks within 20 m of it (Appendix Table 3). A sixth float rock example occurs near the Voltaire outcrop and two more near the summit region (Fig. 1). One of these, named Ian Clough, appears darker and less dusty than most other Keystone Subclass examples, although it retains some of the spectral characteristics of dust ("roll-off" above 1300 cm^{-1} and an emissivity peak near 1650 cm^{-1}). It displays similar low wavenumber features but also clearly shows a peak at ~1080 cm^{-1} consistent with plagioclase and common to Wishstone Subclass (Fig. 4). Consequently, this rock more clearly links Keystone Subclass spectrally to Wishstone Subclass. It also suggests that the lack of this feature in other members of Keystone Subclass may be due to masking effects of dust and soil contaminants present among the rough textural elements of these rocks. Six examples of Keystone targets are shown in Figure 5.

Keel Subclass. Intermediate in alteration between Watchtower and Keystone Subclasses as determined from MB results (Morris et al. 2008), Keel Subclass was first encountered at the Jibsheet Ridge outcrop on sol 481 where two targets were measured with the IDD instruments. Two more examples were measured with the IDD instruments on the Husband Hill summit (Hillary) and one at the Kansas outcrop east of the summit (Fig. 1). All IDD measurements of Keel Subclass were made on outcrops.

Mini-TES observed the Keel target, which serves as the type example. It shares features of both Wishstone and Watchtower Subclasses, most notably with recognizable plagioclase features producing a peak at ~1080 cm^{-1} and a narrow trough at ~540 cm^{-1} (Fig. 5d). The region <600 cm^{-1} displays a broad negative slope similar to Watchtower Subclass (see below) but with weak features superimposed. In some cases, an inflection at ~470 cm^{-1} typical of this class is a fully resolved local minimum. We used the broad negative slope and the presence of a recognizable plagioclase feature at ~540 cm^{-1}, even where it is just an inflection point, to classify Mini-TES targets as Keel Subclass. Forty examples were observed, dominated by outcrop targets of the Hillary summit region, with additional outcrop examples on Jibsheet Ridge and Larry's Outcrop, and a float rock example in the vicinity of the Voltaire outcrop (Fig. 1; Appendix Table 4). Six examples of Keel Subclass are shown in Figure 5.

To the east of the summit is a flat-lying outcrop known as Kansas (Fig. 1) that was classified as Keel Subclass based on APXS/MB measurements (Ming et al. 2008). Although very dusty, the outcrop had portions clean enough to reveal features other than dust in Mini-TES spectra. Three targets (including Lousewort in Fig. 5) present features that are most similar to Keel Subclass although with some differences at the lowest wavenumbers (Fig. 4d). Because of the marginal spectral quality due to dust and the limited exposure, we grouped these targets into the Keel Subclass rather than identifying a new subclass.

Watchtower Subclass. Four examples of Watchtower Subclass were measured with the IDD instruments, all on the Larry's Lookout/Larry's Outcrop part of the feature known as Cumberland Ridge adjacent to the Tennessee Valley (Fig. 1). Mini-TES measured Watchtower rock, which serves as the type example. A strongly negative slope in emissivity with no recognizable plagioclase features dominates the range <600 cm^{-1} and distinguishes the Watchtower Subclass (Fig. 5e). However, a weak emissivity peak near 1080 cm^{-1} likely is attributable to plagioclase. There are 25 targets that show the spectral features of the type example, most of which occur in outcrop at Larry's Lookout/Larry's Outcrop and Jibsheet Ridge (Appendix Table 5). Six examples are shown in Figure 5. No examples of Watchtower Subclass have been recognized farther up Husband Hill or beyond, making it the most spatially confined of the Wishstone-Watchtower suite.

Bruce: A Candidate Watchtower Subclass end-member. Among the rocks observed by Mini-TES and Pancam on Husband Hill is one whose spectrum qualifies as Watchtower Subclass based on its similar low wavenumber characteristics, but that also displays distinctive features that set it apart. Named after Mount Everest explorer Charles Bruce, it occurs as an angular piece of float rock with a maximum length of ~40 cm near the Hillary outcrop on the Husband Hill summit (Fig. 1). It is notably dark and relatively dust-free, with a vaguely striated surface texture that is similar to that observed on other Hillary rocks (Fig. 7). Its minimal dust cover, warm surface temperature (~278 K), and late afternoon acquisition time (16:20) provided optimal measurement conditions, yielding a high quality spectrum well suited to detailed analysis. It displays the strongly negative slope in emissivity at low wavenumbers common to Watchtower Subclass but includes a distinct, relatively broad minimum centered at ~ 460 cm^{-1} and weak peaks at ~1080 and ~1150 cm^{-1} that are above the noise level, identified as 1-sigma variations of the 200 individual spectra in the observation (Fig. 4f).

Bruce most closely resembles another Watchtower Subclass spectrum from a minimally dusty float rock named Cadge on Larry's Outcrop (Figs. 5 and 8). This similarity appears to provide a spectral link between the Bruce float rock and materials comprising Larry's Lookout/Outcrop, which hosts the Watchtower Subclass type-example. No IDD measurements were acquired on Bruce. The range of spectral variations evident in the Watchtower Subclass, represented by the Watchtower type example and Cadge in Figure 8, appears to show a trend toward the features of Bruce, which may indicate that it is a spectral end-member. Given that the chemistry and mineralogy of Watchtower Subclass rocks have been shown to be indicative of substantial alteration (e.g., Hurowitz et al. 2006), Bruce may be an alteration end-member.

RESULTS: MINERALOGY AND ALTERATION CHARACTERISTICS

Previous work demonstrated an alteration trend beginning with the least altered Wishstone Class followed by Keystone, Keel, and Watchtower Subclasses (Hurowitz et al. 2006; Ming et al. 2006; Morris et al. 2006). This trend also is evident in Mini-TES spectra as shown most clearly in a plot of the average of the best examples from each subclass (Fig. 9). The best examples are those spectra that display the greatest spectral contrast and a relatively strong ~667 cm^{-1} atmospheric CO_2 absorption feature indicative of a target much warmer than the atmosphere (Ruff et al. 2006). Under these conditions, the emission from optically thin surface dust is minimized. Although the emission of the rock is still modulated by the dust, the rock's emissivity features are more discernible than when dust emission dominates. The average spectrum of the new M80 Subclass and the candidate Watchtower spectral end-member Bruce also are included in Figure 9. Because the Keystone Subclass rocks are substantially dust contaminated, the original average spectrum is shown along with one incorporating a dust correction. In this case, we found that subtracting 10% of optically thick surface dust is sufficient to remove the recognizable dust features at high wavenumbers. It is this version that was used in subsequent analyses.

The alteration trend evident in the Mini-TES spectra is manifested as a loss of the recognizable plagioclase features in the low wavenumber range (<600 cm^{-1}) with the development of an increasingly negative slope. In the middle wavenumber range (~800-1250 cm^{-1}), there is a trend toward a relatively symmetric U- or V-shaped broad emissivity minimum. The spectrum of Bruce appears to be a culmination of these spectral trends, supporting the idea that it could be an alteration end-member.

Application of FATT to the various subclasses did not identify any independently varying components within the subclasses, unlike that observed in the study of Adirondack class olivine basalts (Hamilton and Ruff 2012). However, analysis of the entire Wishstone-Watchtower series resulted in some interesting and unexpected insights. Four plagioclase target spectra with a compositional range of An_{48} to An_{63} are the best modeled targets of any of the primary igneous phases in the library (Fig. 10a). The quality of fit is inferior to that produced by linear least squares modeling, but this simply means that plagioclase in isolation is not varying across all subclasses. Instead, the recurrence of essentially the same spectral shape recovered from the plagioclase target spectra is perhaps an indication of a dominant feldspar-like spectral component that is independently varying. This is consistent with linear least squares results described in subsequent sections. Other target spectra with similar quality of fit include K-rich obsidian glass and two zeolites that resemble it. As with the feldspar targets, the recovered shapes are not identical to the target spectra, but they are suggestive of a higher SiO_2 (>~55 wt%) amorphous component based on the position and shape of the two emissivity band minima (Fig. 10b).

Target spectra of natural and synthetic basaltic glasses and maskelynite (shocked feldspar glass) recovered spectral shapes suggestive of a lower SiO_2 (<~55 wt%) amorphous component (Fig. 10c). The spectra of the lower silica component are distinguishable from those of the higher silica component in several ways (Fig 11a): 1) the Si-O stretching band minimum is at ~990 cm^{-1} in the lower silica spectra versus ~1075 cm^{-1} in the higher silica recovered spectra, 2) the Si-O stretching band shape in the lower silica recovered spectra is broader than that in the higher silica recovered spectra, and 3) the Si-O bending band minima exhibit notably different shapes, with the lower silica variant having a broader, asymmetric minimum without a distinctive maximum at 400 cm^{-1} and the higher silica variant displaying a narrower, relatively symmetric minimum with a maximum at ~400 cm^{-1}. Similar trends have been observed in spectra of laboratory silicate glasses having variable SiO_2 wt% (Minitti and Hamilton 2010).

Finally, it is worth noting that the recovered lower silica spectral shape cannot be reproduced by a mixture of the plagioclase-like and higher silica spectra. However, a simple additive spectral mixture of equal fractions of the lower and higher silica spectral shapes yields a spectrum that is similar to the Bruce spectrum (Fig. 11b). This lends support both to the FATT modeling results and that Bruce is a possible spectral end-member. The two recovered spectral shapes thus suggest that among the full suite of Mini-TES rock classes are possibly two mineralogical components that vary independently and resemble amorphous silicates of differing SiO_2 content.

Wishstone Subclass mineralogy

We applied linear least squares modeling to the best average Wishstone Subclass spectrum using the NNLS linear retrieval algorithm of Rogers and Aharonson (2008). The spectral results are shown in Fig. 12a with spectral components identified in Table 2. Although the overall fit is good, it is important to recognize that even minor misfit portions can be recognized as misidentified components (Rogers and Aharonson 2008). One example is a weak emissivity peak near 1140 cm^{-1} in the model that is stronger and shifted to lower wavenumber than one in the Wishstone Subclass spectrum. None of the modeled spectral components displays a feature in this position. Instead, it arises from the modeled anhydrite component where a steep increase in emissivity starting at ~1160 cm^{-1} combines with decreasing or flat emissivity of most other components (Fig. 12a). Rerunning the algorithm without anhydrite results in the disappearance of the ~1140 cm^{-1} peak but introduces new misfit at higher wavenumbers due to a near doubling of the kieserite component that is the next best spectral substitute for anhydrite. This suggests either that the available sulfate end-member spectra are insufficient to properly model sulfate(s) in the Wishstone Subclass spectrum or that sulfates are substituting for some other spectral component in this region, as was considered in previous work by Hamilton and Ruff (2012).

Other areas of misfit in the model (Fig. 12a) indicate additional inaccuracies in the modeled components. Only plagioclase is identified confidently, in part because of feature matching as shown in Figure 3. Two separate plagioclase components are modeled, bytownite at 25% and oligoclase at 12% (Table 2). These may represent two distinct phases or perhaps zoned plagioclase (Milam et al. 2004). Bytownite has a modeled uncertainty of ±15%, which is high relative to its modeled abundance. This may be an indication that the available bytownite spectrum is not optimal.

M80 Subclass mineralogy

Because of the pronounced spectral similarities between M80 Subclass and Wishstone Subclass, a good overall fit is achieved using nearly 50% of the average Wishstone Subclass spectrum in the model (Fig. 12b and Table 3). However the key features distinguishing the two subclasses are not well fit. Weak emissivity peaks near 900 cm^{-1} and 520 cm^{-1} are not present in the model, an indication that the end-member library is insufficient to fully model the data. Also, the model introduces more pronounced plagioclase-related peaks at ~490 and 455 cm^{-1} where they are muted in the data (Fig. 12b). A second run of the algorithm without the Wishstone Subclass end-member resulted in a 70% increase in RMS error (Table 3). The key distinguishing spectral features of M80 Subclass again were not properly modeled. Although the model results are insufficient to confidently identify the mineral components that distinguish M80 from Wishstone Subclass, plagioclase likely remains the dominant component. A reduction in olivine is evident based on visual inspection (reduced absorption near 900 cm^{-1}) and model results (Table 3).

Keystone Subclass mineralogy

The notably flat emissivity at low wavenumbers (<550 cm^{-1}) that distinguishes Keystone Subclass from the others is well fit in a model dominated by the Wishstone Subclass average spectrum (~41%) followed by two basaltic glass spectra totaling ~11% (Fig. 12c and Table 4). Two sulfate spectra totaling 7% round out the largest components, excluding the non-rock spectral components. A second run of the algorithm without the Wishstone Subclass end-member resulted in a ~70% increase in RMS error. The anhydrite related erroneous peak near 1140 cm^{-1} is present in this second model along with degradation in the quality of the fit at low wavenumbers (Fig. 12c). The good fit of this low wavenumber range achieved using the Wishstone end-member and the two glass components suggests that the difference between Wishstone and Keystone Subclasses is due to the addition of one or more components that resemble basaltic glass. Basaltic glass has a relatively deep and featureless absorption centered at ~450 cm^{-1} that combines with the plagioclase features of Wishstone Subclass to create the characteristic shape of Keystone Subclass in this spectral range (Fig. 12c).

Keel Subclass mineralogy

The modeling of Keel Subclass resulted in a remarkably good fit, the best among any of the spectral classes presented in this work (Fig. 12d). Despite the visually disparate spectral features between Wishstone and Keel, the former still appears in the model as the dominant component at 23% (Table 5). This model is the first case where the Bruce spectrum appears as a major component, at 19%. Basaltic glass is the next largest component at 5% (excluding non-rock components), which because of its relatively high spectral contrast, makes a substantive contribution to the fit; likewise for the modeled oligoclase at 4%. It is perhaps noteworthy that 11 of the modeled components occur at <1%, so the quality of the fit is due in part to the sum of many minor additional components. However, we interpret the substantive components as an indication that Wishstone Subclass could be the parent rock type of Keel Subclass with alteration represented by a Bruce-like spectral component augmented by lesser components.

A second run of the algorithm without the Wishstone and Bruce end-members resulted in a ~75% increase in RMS error (Table 5). However, this is a case where the fit of the first model run is so good that even with the substantial increase in RMS error of the second run, the quality of the fit is still good (Fig. 12d). The spectrally dominant components of this second run, excluding the non-rock components, are basaltic glass, oligoclase, and anhydrite. Although anhydrite has a modeled abundance of only 2%, its high spectral contrast results in a substantial contribution even at this low abundance. The modeled shocked anorthite component has higher abundance (8%), but with its low contrast, is nearly indiscernible at this abundance. In this run, Keel Subclass presents the plagioclase-rich aspect of Wishstone Subclass combined with a basaltic glass-like component (Table 5). Uncertainty remains about the robustness of sulfate identification (cf. Hamilton and Ruff 2012).

Watchtower Subclass mineralogy

Although Watchtower Subclass is spectrally similar to Keel Subclass, the quality of the model fit is inferior, most notably at low wavenumbers (<550 cm^{-1})(Fig. 12e). Wishstone Subclass is present as a component in the best-fit model at 30%, followed by two basaltic glass components totaling 21% (Table 6). A higher-silica K-rich glass component is the next most abundant at 3% (excluding the non-rock components) but with its high-contrast spectrum, provides a substantive contribution to the fit even at this low abundance. The Bruce component is modeled at a comparable value, but because of its lower contrast, it makes only a small contribution to the fit.

Removing the Wishstone and Bruce end-members from the library results in a 27% increase in RMS error, a relatively small change. The quality of fit at low wavenumbers is comparable to the first run, but visibly degraded at higher wavenumbers, most notably with a weak emissivity peak near 1140 cm^{-1} (Fig. 12e) attributable to the high-contrast anhydrite component (4%) as described above. Two basaltic glass components totaling 25% dominate the model, with oligoclase following at 8% (Table 6). Although saponite is the next highest at 5%, it is spectrally a low contrast phase such that its identification cannot be considered robust at this abundance. Instead, we interpret the basaltic glass components as proxies for one or more amorphous alteration phases, given that Watchtower Subclass is recognized as the most altered among the rocks measured with the APXS and MB instruments (Hurowitz et al. 2006; Ming et al. 2006; Morris et al. 2006).

Bruce mineralogy

The modeling of Bruce is the only case where Wishstone Subclass is not the dominant component, replaced instead by saponite at 16% (Table 7). The Wishstone component appears as the fourth most abundant at 7%, but with a notably high uncertainty value of 6%. A second run without Wishstone in the library resulted in a negligible increase in RMS error (~1%). In both cases, the overall fit is good but in detail there are clear examples of misfit that indicate an end-member library insufficient to capture one or more components (Fig. 12f). Key features of Bruce that are misfit by the models include: the narrow minimum of the strong V-shape centered at ~1025 cm^{-1}; a weak narrow peak at ~1150 cm^{-1}; the nearly featureless drop in emissivity to a broad minimum centered at ~460 cm^{-1}; and the adjacent peak at ~415 cm^{-1}. Both models display much more fine scale structure in this low wavenumber range than is present in the Bruce spectrum, which emphasizes that some of the modeled components are inaccurate.

The dominant modeled saponite component broadly resembles the Bruce spectrum with two strong absorption features in roughly the same positions as those of Bruce (Fig. 12f). But the shapes of these features are different than those of Bruce, with minima that are broader. Because saponite lacks sharp spectral features akin to plagioclase for example, it is not clearly recognizable visually in the Bruce spectrum. Saponite is thus a possible but not robustly identified component.

Summary of mineralogic results

Plagioclase and various amorphous silicate phases in differing amounts are the dominant spectral components of the different rock classes. Despite the recognized inaccuracies of the linear least squares modeling in some cases, these major components display trends with alteration as shown by the normalized values in which the dust, slope, and blackbody components are removed. Table 8 tallies the changes in abundance of plagioclase and amorphous silicate totals among the modeled rock classes arranged from least to most altered as determined by previous MB results shown by increasing values of npOx, Fe^{3+}/Fe_T, and MAI. With the exception of Bruce, modeled plagioclase abundance decreases and amorphous silicate abundance increases with increasing alteration. These trends are consistent with visually recognizable changes in the spectra as shown by Figure 9.

The modeling results do not present a clear mixing trend between Wishstone Subclass and Bruce. For example, although Keel Subclass is best modeled using a combination of both, Watchtower Subclass requires little of the Bruce component to achieve the best fit despite having the most Bruce-like spectral characteristics in the low wavenumber range. Although Bruce does not appear to be a common component of the altered subclasses, Wishstone Subclass is the largest component of the best-fit models of M80, Keystone, Keel, and Watchtower Subclass spectra. These results are discussed below.

DISCUSSION

Our results support the MB-based subdivision of Watchtower Class into three subclasses (Keystone, Keel, and Watchtower)(Morris et al. 2006; Morris et al. 2008). This is noteworthy given that the Keystone and Keel Subclasses were not considered separable based on APXS geochemistry. Furthermore, the evidence for increasing alteration among these subclasses shown by increasing values of npOx, Fe^{3+}/Fe_T, and MAI coincides with decreasing plagioclase and increasing amorphous silicate abundance determined with Mini-TES (Table 8). No singular amorphous silicate phase is modeled in the Mini-TES spectra. Instead, various combinations of different basaltic glasses and shocked plagioclase are modeled that likely represent proxies for one or more alteration phases that are not present in the spectral library. Combined with the MB results, it appears that the alteration includes npOx either as a separate component or perhaps attributable to the amorphous silicate component.

The increasing amorphous silicate component coincident with increasing alteration appears to support the idea that this component results from alteration that either masked or altered the plagioclase component among these rocks. Given that Wishstone Subclass, with its strong plagioclase spectral features, is the largest component of the best-fit models of all the subclasses except Bruce, one interpretation is that these subclasses represent Wishstone-like starting lithology that has been increasingly altered. An alternative hypothesis is that the Wishstone-Watchtower series represents plagioclase-rich pyroclastic rocks with variable amounts of primary basaltic glass. Over time, the glass is altered while the plagioclase is largely unaltered.

This would lead to the appearance of increasing alteration with decreasing plagioclase abundance.

Observations from elsewhere in Gusev crater provide clues that may help to distinguish between the two hypotheses. A rock known as Mazatzal on the rim of Bonneville crater visited by Spirit on the plains adjacent to the Columbia Hills displays unambiguous evidence of a coating attributed to alteration (e.g., Squyres et al. 2004; Haskin et al. 2005). Here, all the rocks appear to be olivine-rich Adirondack Class basalt (e.g., Squyres et al. 2004; Ruff et al. 2006; Hamilton and Ruff 2012). The thin (<1 mm) coating has notably similar Mini-TES spectral characteristics as those of Keel and Watchtower Subclasses (Fig. 13). The coating is sufficiently opaque in the spectral range of Mini-TES to completely mask the strong, low wavenumber features of the dominant olivine component in the underlying Adirondack Class basalt (Hamilton and Ruff 2012). Basaltic glass is the dominant modeled spectral component of the Mazatzal coating although it was viewed as a proxy for an alteration component atypical of terrestrial weathering rinds (Hamilton and Ruff 2012). Comparable coatings are not evident in images of Keel and Watchtower Subclass rocks, but the Mazatzal coating demonstrates a style of alteration in which the spectral characteristics of the host rock are masked by an amorphous silicate of basaltic composition. Perhaps alteration of Wishstone-like rocks has resulted in progressive masking of their spectral characteristics by a comparable amorphous silicate component.

The FATT-recovered spectral shapes provide additional insight into the nature of the amorphous component. The spectral shapes that resemble higher and lower SiO_2 amorphous components (Figs. 10b,c and 11a) may indicate two separate amorphous (or dominantly amorphous) components in the Wishstone-Watchtower series. Bruce may represent a combination of these amorphous components that is not consistent among the other subclasses, thus not modeled consistently among them. It still may represent a compositional end-member. The presence of the lower SiO_2 component was recognized in previous linear least squares modeling as a basaltic glass in Watchtower (Ruff et al. 2006). The presence of a higher SiO_2 component was not recognized previously.

Just as informative as the spectral shapes that were recovered from FATT are the shapes that were not recovered. Target spectra representing pyroxenes, olivines, sulfates, and oxides did not result in the recovery of similar shapes, suggesting that these phases, which have been inferred on the basis of MB and APXS data (Ming et al. 2006; Morris et al. 2006), do not vary independently across the Wishstone-Watchtower series. In other words, although these phases likely are present, they vary roughly in unison with other phases.

IMPLICATIONS

Our results demonstrate that the alteration of Wishstone Class rocks is manifested as an increase of an amorphous silicate component, as shown by Mini-TES measurements, and increased Fe^{3+} in the form of npOx, as shown by MB measurements. The oxidative weathering of rocks in the McMurdo Dry Valleys of Antarctica has been shown to produce similar manifestations (Salvatore et al. 2013), making oxidative weathering a candidate process. However, this process does not result in the notably high values of Fe^{3+}/Fe_T and npOx such as those seen among the Wishstone-Watchtower rocks. An alternative process involving acid fog has been suggested on the basis of textural variations among the subclasses (Cole 2015). However, laboratory experiments intended to mimic acid fog alteration produced phyllosilicate and/or opaline silica phases (Tosca et al. 2004), which have not been identified with confidence in our work.

We hypothesize that a water-limited alteration process is possible in the extreme aridity and cold of Mars that is sufficient to depolymerize silicate tetrahedral networks but insufficient to allow significant cation mobility. On Earth, silicate depolymerization is recognized as a rate-limiting step in natural and experimental weathering studies (e.g., Banfield and Barker 1994; Banfield et al. 1995), which perhaps leads to persistent amorphous silicate phases in the Martian environment. The apparent absence of any phyllosilicate or opaline silica phases among the alteration products supports the concept of limited cation mobility and is perhaps consistent with a form of "cation conservative" alteration as has been described for other rocks in Gusev crater (Hurowitz and Fischer 2014).

Viewed in this context, the results of the first XRD measurements on Mars by the CheMin instrument on the Curiosity rover become more significant. Samples of drifted soil from the Rocknest sand shadow in Gale crater have a crystalline component dominated by a plagioclase phase (~An_{57}) with no recognized crystalline secondary silicates but as much as 45 wt% amorphous material that is best modeled by basaltic glass (Bish et al. 2013; Blake et al. 2013). Those investigators suggested that the amorphous material was not necessarily basaltic glass but could instead be analogous to the substantial abundances of npOx in Gusev crater soils. A true basaltic glass component is unlikely based on chemical constraints that appear to preclude such composition (Dehouck et al. 2014) and that support indications of other amorphous alteration products (McAdam et al. 2014; Sklute et al. 2015). The alteration of Wishstone-Watchtower rocks manifests as a lack of phyllosilicates but with abundant npOx associated with an amorphous component that spectrally resembles basaltic glass, characteristics apparently in common with Rocknest sand. The presence of such comparable material in widely separated locations suggests that the style of alteration encountered by the Spirit rover on Husband Hill is not limited to this location, but may be common elsewhere on the surface of Mars.

Acknowledgements

This work was funded by the NASA Mars Data Analysis program, for which we are grateful. We thank Brad Jolliff for organizing the special issue of which this paper is a part and overseeing its review. We also thank reviewers Josh Bandfield and Tim Glotch for very thorough and constructive feedback, which substantially improved the quality of the final paper.

References

Arvidson, R.E., Ruff, S.W., Morris, R.V., Ming, D.W., Crumpler, L.S., Yen, A.S., Squyres, S.W., Sullivan, R.J., Bell, J.F., III, Cabrol, N.A., and others. (2008) Spirit Mars Rover mission to the Columbia Hills, Gusev Crater: Mission overview and selected results from the Cumberland Ridge to Home Plate. Journal of Geophysical Research, 113(E12S33), doi:10.1029/2008JE003183.

Arvidson, R.E., Squyres, S.W., Anderson, R.C., Bell, J.F., III, Blaney, D., Bruckner, J., Cabrol, N.A., Calvin, W.M., Carr, M.H., Christensen, P.R., and others. (2006) Overview of the Spirit Mars Exploration Rover Mission to Gusev Crater: Landing site to Backstay Rock in the Columbia Hills. Journal of Geophysical Research, 111(E02S01), doi:10.1029/2005JE002499.

Bandfield, J.L., Christensen, P.R., and Smith, M.D. (2000a) Spectral data set factor analysis and end-member recovery: Application to analysis of Martian atmospheric particulates. Journal of Geophysical Research, 105(E4), 9573-9587.

Bandfield, J.L., Hamilton, V.E., and Christensen, P.R. (2000b) A global view of Martian volcanic compositions from MGS-TES. Science, 287, 1626-1630.

Banfield, J.F., Ferruzzi, G.G., Casey, W.H., and Westrich, H.R. (1995) HRTEM study comparing naturally and experimentally weathered pyroxenoids. Geochimica et Cosmochimica Acta, 59(1), 19-31.

Banfield, J.L., and Barker, W.W. (1994) Direct observation of reactant-product interfaces formed in natural weathering of exsolved, defective amphibole to smectite: Evidence for episodic, isovolumetric reactions involving structural inheritance. Geochimica et Cosmochimica Acta, 58(5), 1419-1429.

Bell, J.F., III, Joseph, J., Sohl-Dickstein, J.N., Arneson, H.M., Johnson, M.J., Lemmon, M.T., and Savransky, D. (2006) In-flight calibration and performance of the Mars Exploration Rover Panoramic Camera (Pancam) Instruments. Journal of Geophysical Research, 111(E02S03), doi:10.1029/2005JE002444.

Bish, D.L., Blake, D.F., Vaniman, D.T., Chipera, S.J., Morris, R.V., Ming, D.W., Treiman, A.H., Sarrazin, P., Morrison, S.M., Downs, R.T., and others. (2013) X-ray diffraction results from Mars Science Laboratory: Mineralogy of Rocknest at Gale crater. Science, 341, 1-5.

Blake, D.F., Morris, R.V., Kocurek, G., Morrison, S.M., Downs, R.T., Bish, D.L., Ming, D.W., Edgett, K.S., Rubin, D., Goetz, W., and others. (2013) Curiosity at Gale Crater, Mars: Characterization and analysis of the Rocknest sand shadow. Science, 341, 1-7.

Changela, H.G., and Bridges, J.C. (2011) Alteration assemblages in the nakhlites: Variation with depth on Mars. Meteoritics and Planetary Science, 45(12), 1847-1867.

Christensen, P.R., Bandfield, J.L., Clark, R.N., Edgett, K.S., Hamilton, V.E., Hoefen, T., Kieffer, H.H., Kuzmin, R.O., Lane, M.D., Malin, M.C., and others. (2000) Detection of crystalline hematite mineralization on Mars by the Thermal Emission Spectrometer: Evidence for near-surface water. Journal of Geophysical Research, 105(E4), 9623-9642.

Christensen, P.R., Mehall, G.L., Silverman, S.H., Anwar, S., Cannon, G., Gorelick, N., Kheen, R., Tourville, T., Bates, D., Ferry, S., and others. (2003) Miniature Thermal Emission Spectrometer for the Mars Exploration Rovers. Journal of Geophysical Research, 108(E12, 8064), doi:10.1029/2003JE002117.

Christensen, P.R., Ruff, S.W., Fergason, R.L., Knudson, A.T., Anwar, S., Arvidson, R.E., Bandfield, J.L., Blaney, D.L., Budney, C., Calvin, W., and others. (2004) Initial Results from the Mini-TES Experiment in Gusev Crater from the Spirit Rover. Science, 305, 837-842.

Clark, B.C., Arvidson, R.E., Gellert, R., Morris, R.V., Ming, D.W., Richter, L., Ruff, S.W., Michalski, J.R., Farrand, W.H., Yen, A.S., and others. (2007) Evidence for montmorillonite or its compositional equivalent in Columbia Hills, Mars. Journal of Geophysical Research, 112(E06S01).

Cole, S. (2015) In-situ evidence for alteration by acid fog on Husband Hill, Gusev crater, Mars. Geological Society of America Abstracts, 47(7), 268, No. 94-10.

Dehouck, E., McLennan, S.M., Meslin, P.-Y., and Cousin, A. (2014) Constraints on abundance, composition, and nature of X-ray amorphous components of soils and rocks at Gale crater, Mars. Journal of Geophysical Research, 119, 2640-2657.

Feely, K.C., and Christensen, P.R. (1999) Quantitative compositional analysis using thermal emission spectroscopy: Application to igneous and metamorphic rocks. Journal of Geophysical Research, 104(E10), 24195-24210.

Glotch, T.D., and Bandfield, J.L. (2006) Determination and interpretation of surface and atmospheric Mini-TES spectral end-members at the Meridiani Planum landing site. Journal of Geophysical Research, 111(E12S06), doi: 10.1029/2005JE002671.

Glotch, T.D., Bandfield, J.L., Christensen, P.R., Calvin, W.M., McLennan, S.M., Clark, B.C., Rogers, A.D., and Squyres, S.W. (2006) Mineralogy of the light-toned outcrop at Meridiani Planum as seen by the Miniature Thermal Emission Spectrometer and implications for its formation. Journal of Geophysical Research, 111(E12S03), doi:10.1029/2005JE002672.

Glotch, T.D., and Rogers, A.D. (2013) Evidence for magma-carbonate interaction beneath Syrtis Major, Mars. Journal of Geophysical Research, 118, 126-137.

Gorevan, S.P., Myrick, T., Davis, K., Chau, J.J., Bartlett, P., Mukherjee, S., Anderson, R., Squyres, S.W., Arvidson, R.E., Madsen, M.B., and others. (2003) Rock Abrasion Tool: Mars Exploration Rover mission. Journal of Geophysical Research, 108(E12, 8068), doi:10.1029/2003JE002061.

Hamilton, V.E., and Christensen, P.R. (2000) Determining the modal mineralogy of mafic and ultramafic igneous rocks using thermal emission spectroscopy. Journal of Geophysical Research, 105, 9717-9733.

Hamilton, V.E., and Ruff, S.W. (2012) Distribution and characteristics of Adirondack-class basalt as observed by Mini-TES in Gusev crater, Mars and its possible volcanic source. Icarus, 218(2), 917-949.

Haskin, L.A., Wang, A., Jolliff, B.L., McSween Jr., H.Y., Clark, B.C., Des Marais, D.J., McLennan, S.M., Tosca, N.J., Hurowitz, J.A., Farmer, J.D., and others. (2005) Water alteration of rocks and soils on Mars at the Spirit rover site in Gusev crater. Nature, 436, 66-69.

Heiken, G.H. (1971) Tuff rings: Examples from the Fort Rock-Christmas Lake Valley Basin, south-central Oregon. Journal of Geophysical Research, 76(23), 5615-5626.

Horgan, B., and Bell III, J.F. (2012) Widespread weathered glass on the surface of Mars. Geology, 40(5), 391-394.

Hurowitz, J.A., and Fischer, W.W. (2014) Contrasting styles of water–rock interaction at the Mars Exploration Rover landing sites. Geochimica et Cosmochimica Acta, 127, 25-38.

Hurowitz, J.A., McLennan, S.M., McSween Jr., H.Y., DeSouza Jr., P.A., and Klingelhöfer, G. (2006) Mixing relationships and the effects of secondary alteration in the Wishstone and

Watchtower Classes of Husband Hill, Gusev Crater, Mars. Journal of Geophysical Research, 111(E12S14).

Leshin, L.A., Mahaffy, P.R., Webster, C.R., Cabane, M., Coll, P., Conrad, P.G., Archer Jr., P.D., Atreya, S.K., Brunner, A.E., Buch, A., and others. (2013) Volatile, isotope, and organic analysis of Martian fines with the Mars Curiosity Rover. Science, 341.

McAdam, A.C., Franz, H.B., Sutter, B., Archer Jr., P.D., Freissinet, C., Eigenbrode, J.L., Ming, D.W., Atreya, S.K., Bish, D.L., Blake, D.F., and others. (2014) Sulfur-bearing phases detected by evolved gas analysis of the Rocknest aeolian deposit, Gale Crater, Mars. Journal of Geophysical Research, 119, 373-393.

Milam, K.A., McSween Jr., H.Y., Hamilton, V.E., Moersch, J.E., and Christensen, P.R. (2004) Accuracy of plagioclase compositions from laboratory and Mars spacecraft thermal emission spectra. Journal of Geophysical Research, 109(E04001).

Ming, D.W., Gellert, R., Morris, R.V., Arvidson, R.E., Bruckner, J., Clark, B.C., Cohen, B.A., d'Uston, C., Economou, T., Fleischer, I., and others. (2008) Geochemical properties of rocks and soils in Gusev Crater, Mars: Results of the Alpha Particle X-Ray Spectrometer from Cumberland Ridge to Home Plate. Journal of Geophysical Research, 113(E12S39), doi:10.1029/2008JE003195.

Ming, D.W., Mittlefehldt, D.W., Morris, R.V., Golden, D.C., Gellert, R., Yen, A.S., Clark, B.C., Squyres, S.W., Farrand, W.H., Ruff, S.W., and others. (2006) Geochemical and mineralogical indicators for aqueous processes in the Columbia Hills of Gusev crater, Mars. Journal of Geophysical Research, 111(E02S12), doi:10.1029/2005JE002560.

Minitti, M.E., and Hamilton, V.E. (2010) A search for basaltic-to-intermediate glasses on Mars: Assessing martian crustal mineralogy. Icarus, 210, 135-149.

Morris, R.V., Klingelhofer, G., Schroder, C., Fleischer, I., Ming, D.W., Yen, A.S., Gellert, R., Arvidson, R.E., Rodionov, D.S., Crumpler, L.S., and others. (2008) Iron mineralogy and aqueous alteration from Husband Hill through Home Plate at Gusev Crater, Mars: Results from the Mo¨ssbauer instrument on the Spirit Mars Exploration Rover. Journal of Geophysical Research, 113(E12S42), doi:10.1029/2008JE003201.

Morris, R.V., Klingelhofer, G., Schroder, C., Rodionov, D.S., Yen, A.S., Ming, D.W., de Souza, P.A., Jr., Fleischer, I., Wdowiak, T., Gellert, R., and others. (2006) Mössbauer mineralogy of rock, soil, and dust at Gusev crater, Mars: Spirit's journey through weakly altered olivine basalt on the plains and pervasively altered basalt in the Columbia Hills. Journal of Geophysical Research, 111(E02S13), doi:10.1029/2005JE002584.

Ramsey, M.S., and Christensen, P.R. (1998) Mineral abundance determination: Quantitative deconvolution of thermal emission spectra. Journal of Geophysical Research, 103, 577-596.

Rivera-Hernandez, F., Bandfield, J.L., Ruff, S.W., and Wolff, M.J. (2015) Characterizing the thermal infrared spectral effects of optically thin surface dust: Implications for remote-sensing and in situ measurements of the martian surface. Icarus, 262, 173-186.

Rogers, A.D., and Aharonson, O. (2008) Mineralogical composition of sands in Meridiani Planum determined from Mars Exploration Rover data and comparison to orbital measurements. Journal of Geophysical Research, 113(E06S14), doi:10.1029/2007JE002995.

Ruff, S.W., and Bandfield, J.L. (2010) Refinement and discovery with Mini-TES spectra in Gusev crater. Lunar and Planetary Science Conference, 41, Abstract #2411.

Ruff, S.W., Christensen, P.R., Blaney, D.L., Farrand, W.H., Johnson, J.R., Michalski, J.R., Moersch, J.E., Wright, S.P., and Squyres, S.W. (2006) The rocks of Gusev Crater as viewed by the Mini-TES instrument. Journal of Geophysical Research, 111(E12S18), doi:10.1029/2006JE002747.

Ruff, S.W., Farmer, J.D., Calvin, W.M., Herkenhoff, K.E., Johnson, J.R., Morris, R.V., Rice, M.S., Arvidson, R.E., Bell, J.F., III, Christensen, P.R., and others. (2011) Characteristics, distribution, origin, and significance of opaline silica observed by the Spirit rover in Gusev Crater. Journal of Geophysical Research, 116(E00F23).

Salvatore, M.R., Mustard, J.F., Head, J.W., Cooper, R.F., Marchant, D.R., and Wyatt, M.B. (2013) Development of alteration rinds by oxidative weathering processes in Beacon Valley, Antarctica, and implications for Mars. Geochimica et Cosmochimica Acta, 115, 137-161.

Savransky, D., and Bell III, J.F. (2004) True Color and Chromaticity of the Martian Surface and Sky from Mars Exploration Rover Pancam Observations. Eos Trans. AGU, Abstract P21A-0917.

Sklute, E.C., Jensen, H.B., Rogers, A.D., and Reeder, R.J. (2015) Morphological, structural, and spectral characteristics of amorphous iron sulfates. Journal of Geophysical Research, 120, 809-830.

Smith, M.D., Wolff, M.J., Spanovich, N., Ghosh, A., Banfield, D., Christensen, P.R., Landis, G.A., and Squyres, S.W. (2006) One Martian year of atmospheric observations using MER Mini-TES. Journal of Geophysical Research, 111(E12S13), doi:10.1029/2006JE002770.

Squyres, S.W., Arvidson, R.E., Bell, J.F., III, Bruckner, J., Cabrol, N.A., Calvin, W., Carr, M.H., Christensen, P.R., Clark, B.C., Crumpler, L.S., and others. (2004) The Spirit Rover's Athena science investigation at Gusev Crater, Mars. Science, 305(5685), 794-799.

Squyres, S.W., Arvidson, R.E., Blaney, D.L., Clark, B.C., Crumpler, L.S., Farrand, W.H., Gorevan, S., Herkenhoff, K.E., Hurowitz, J., Kusack, A., and others. (2006) The Rocks of the Columbia Hills. Journal of Geophysical Research, 111(E02S11), doi:10.1029/2005JE002562.

Squyres, S.W., Arvidson, R.E., Ruff, S.W., Gellert, R., Morris, R.V., Ming, D.W., Crumpler, L.S., Farmer, J.D., Des Marais, D.J., Yen, A.S., and others. (2008) Detection of Silica-Rich Deposits on Mars. Science, 320, 1063-1067.

Thomson, J.L., and Salisbury, J.W. (1993) The mid-infrared reflectance of mineral mixtures (7-14 μm). *Remote Sensing of Environment*, *45*, 1-13.

Tosca, N.J., McLennan, S.M., Lindsley, D.H., and Schoonen, M.A.A. (2004) Acid-sulfate weathering of synthetic Martian basalt: the acid fog model revisited. Journal of Geophysical Research, 109(E05003), doi:10.1029/2003JE002218.

Figure Captions

Figure 1. Oblique view of Husband Hill looking south. Red line indicates the traverse path of the Spirit rover entering the scene from the right. Base image and topography are from the High Resolution Imaging Experiment (HiRISE; PSP_001777_1650) and along with the traverse path, were rendered using the Mars feature of Google Earth.

Figure 2. Examples of the spectral effects of optically thin surface dust on rocks. (a) The Wishstone subclass rock called La Brea was observed on three different sols at different times of day producing variations in spectral contrast and band shape. The white circle (inset) represents the approximate field of view (FOV) of Mini-TES with a diameter of ~12 cm shown on a Pancam approximate true color (ATC; Savransky and Bell III 2004; Bell et al. 2006) image (subframe of P2574 acquired on sol 343). All ATC images are available from http://marswatch.astro.cornell.edu/pancam_instrument/true_color.html. Mini-TES spectra are from sol 340, P3816 (black), sol 341, P3820, (red), and sol 347, P3832, (green). (b) Spectra from a Wishstone subclass rock with the two Mini-TES targets called Orange Grove (black spectrum, sol 352, P3842) and Colorado (red spectrum, sol 352, P3843) show pronounced distortions due to the spectral effects of surface dust, most notable in the ~800 to 1300 cm^{-1} range. The Mini-TES FOV circles (colors match spectra) with a diameter of ~15 cm are shown on a Pancam ATC image (subframe of P2589 acquired on sol 352). The grey box in each plot indicates the approximate spectral range over which atmospheric CO_2 features are most evident.

Figure 3. Wishstone Subclass spectrum (black; average of the 10 best Mini-TES spectra) compared with scaled and offset laboratory spectra of feldspars and a basalt sample from Hole in the Ground maar in Oregon collected by Aileen Yingst and Mariek Schmidt. Intermediate

plagioclase (~An_{30-60}) displays a set of features (vertical lines) recognizable in Wishstone Subclass.

Figure 4. Mini-TES spectra grouped by spectral classification. (a) Red spectrum is from the rock Wishstone and the green spectrum is the average of all 59 examples (gray). (b) Red spectrum is from the rock M80 and the green spectrum is the average of all 55 examples (gray). Vertical lines highlight features described in the text. (c) Red spectrum is from the Keystone outcrop (target Madam) and the green spectrum is the average of all 13 examples (gray). The blue spectrum is from the float rock named Ian Clough described in the text. Vertical lines highlight features described in the text. (d) Red spectrum is from the Keel outcrop and the green spectrum is the average of all 40 examples (gray). The three blue spectra are slight variants of Keel Subclass from the outcrop known as Kansas. Vertical lines highlight features described in the text. (e) Red spectrum is from the rock Watchtower and the green spectrum is the average of all 25 examples (gray). (f) Single Bruce spectrum (red) with 1-sigma variations (gray).

Figure 5. Pancam approximate true color images of examples of rocks or outcrops from each spectral subclass. White scale bar is ~15 cm in all images. Sol number and product identifier for each image is shown below.

Figure 6. Watchtower rock before (left) and after (right) the grinding operation by the Rock Abrasion Tool (RAT). The RAT operation appears to have caused small soil avalanches as shown by black arrows and was the last grind because of the resulting heavy wear on the RAT grind heads. Pancam approximate true color images are shown from sol 409 (left) and 419 (right). RAT "hole" is ~4 cm in diameter.

Figure 7. Pancam approximate true color image of the possible Watchtower end-member called Bruce (sol 617 P2597). Maximum dimension is ~40 cm.

This is a preprint, the final version is subject to change, of the American Mineralogist (MSA)
Cite as Authors (Year) Title. American Mineralogist, in press.
(DOI will not work until issue is live.) DOI: http://dx.doi.org/10.2138/am-2017-5618

Figure 8. Mini-TES spectra of Bruce with Watchtower rock and the Watchtower Subclass rock called Cadge (scaled by 65%). Bruce may represent a spectral end-member of the Watchtower Subclass.

Figure 9. Mini-TES subclass spectral averages showing variations from least to most altered rocks (top to bottom). Vertical lines highlight features associated with plagioclase that are most evident in Wishstone. Cyan Keystone spectrum is uncorrected for surface dust.

Figure 10. Target spectra (black) and modeled results (red) using FATT-derived eigenvectors from the full Wishstone-Watchtower series: (a) four plagioclase feldspars (An_{48} to An_{63}); (b) obsidian and two zeolites; and (c) natural and synthetic basaltic glass, and maskelynite.

Figure 11. Results from FATT modeling of Mini-TES spectra. (a) Averages of the modeled results shown in Figure 10. (b) Comparison of the measured spectrum of Bruce (red) with a simple additive mixture of 50% of the FATT-modeled higher silica component and 50% of the lower silica component shown in (a).

Figure 12. Mini-TES measured (black) and linear least squares modeled spectra of the different spectral subclasses, fit between 1350 and 380 cm^{-1}, with the region of atmospheric CO_2 excluded. Model 1 spectra are shown in red and offset in green; model 2 spectra are in blue with an offset. Vertical lines highlight misfit features described in the text. Purple and brown laboratory spectra in (a) represent the modeled abundance of anhydrite and plagioclase, respectively. Purple laboratory spectra in (c) and (f) represent the modeled abundance of basaltic glass and saponite, respectively.

Figure 13. Comparison of the Mini-TES spectrum of the coating on Mazatzal rock from the Gusev crater plains and those of the most altered subclasses of Wishstone-Watchtower rocks. All spectra have been corrected for dust, slope, and blackbody components.

Table 1. Spectra used in FATT and linear least squares (deconvolution) modeling

Category	Name[a]	Category	Name
Plagioclase feldspar	Albite WAR-0612	Phosphate	Wavellite ML-P7
	Oligoclase WAR-0234		Meta-variscite ML-P4
	Andesine BUR-240		Pyromorphite ML-P3
	Labradorite WAR-4524		Apatite ML-P1
	Labradorite WAR-RGAND01	Oxide	Black Hematite Coating[h]
	Bytownite WAR-1384		Magnetite Synthetic Packed Powder MTS5[h]
	Anorthite BUR-340		Goethite Synthetic Packed Powder GTS2[h]
			Ilmenite WAR-4119
Pyroxene	Diopside WAR-6474	Secondary silicate	Serpentine HS-8.4B
	Diopside NMNH-80819		Serpentine BUR-1690
	Hedenbergite, manganoan NMNH-R11524		Kaolinite KGa-1b granular
			Halloysite WAR-5102 solid
	Hedenbergite NMNH-16168		Saponite ASU-SAP01 granular
			Ca-montmorillonite STx-1 solid
	Pigeonite Lindsley $Wo_{10}En_{36}Fs_{54}$ 33,34[b]		Na-montmorillonite SWy-2 granular
			Nontronite WAR-5108 granular
	Enstatite NMNH-R14440		Fe-smectite SWa-1 solid
	Bronzite average		Illite IMt-2 granular
	Hypersthene NMNH-B18247		Heulandite
			Stilbite
Olivine	Forsterite BUR-3720A		Beidellite Sbdl < 0.2 mic[i]
	KI 3115 Fo_{68}[c]		Nontronite Nau-1 < 0.2 mic[i]
	KI 3362 Fo_{60}[c]		Nontronite Nau-2 < 0.2 mic[i]
	KI 3373 Fo_{35}[c]		Hectorite SHca < 0.2 mic[i]
	KI 3008 Fo_{10}[c]		Montmorillonite Swy-1 < 0.2 mic[i]
	Fayalite WAR-RGFAY01		Saponite <0.2 mic[i]
Glass	Silica glass[d]	Sulfate	Gypsum var. Alabaster ML-S11
	K-rich obsidian glass[d]		Anhydrite ML-S9
	Quenched basalt[d]		Celestite ML-S13
	RVM Mars glass[e]		Kieserite KIEDE1 < 1mm[j]
	Basalt glass HWKV340A:		Glauberite GBYAZ1-R1[j]
	Matte uneven surface[e]		Epsomite[j]
	Glassy black flat surface[e]	Other	Slope
	Rind spot		Gusev surface dust (thick dust)[k]
	Maskelynite ASU-7591		Average sky (thin dust 1)[k]
	Shocked An 22.6 GPa[g]		MER A dust shape (thin dust 2)[k]
	Shocked An 37.5 GPa[g]		Wishstone Subclass best average
			Bruce

[a]Unless otherwise noted, spectra are from the ASU TES library (Christensen et al. 2000)
[b]Hamilton et al. 2000 [c]Hamilton 2010 [d]Wyatt et al. 2001 [e]R. V. Morris personal communication [g]Johnson et al. 2002 [h]Glotch et al., 2004 [i]Michalski et al. 2006 [j]Provided by A. Baldridge [k]Hamilton and Ruff 2012

933 **Table 2.** Wishstone Subclass spectral deconvolution results

End-member	Abundance (%)	Uncertainty (± %)	Normalized (%)
Bytownite WAR-1384 177	25	15	25
Pigeonite	13	4	13
Oligoclase BUR-3680 48	12	5	12
Kieserite KIEDE1 < 1mm	11	3	11
Basalt Glassy Black Flat	9	3	9
Olivine KI 3362 Fo60	5	2	6
Anhydrite ML-S9	5	1	5
Kaolinite KGa-1b granular 185	4	6	4
Olivine KI 3008 Fo10	3	2	3
Meta-variscite ML-P4 95	3	1	3
Pyromorphite ML-P3 77	3	3	3
Average enstatite	2	1	2
Apatite ML-P1 86	1	1	1
Glauberite GBYAZ1-R1	1	1	1
Other (1)	<1		<1
Thick dust	17	2	0
Thin dust 1	6	4	0
Thin dust 2	4	1	0
Slope	33	6	0
Blackbody	-47	10	0
Total	111		100
RMS	0.207		

Table 3. M80 Subclass spectral deconvolution results

End-member	Abundance (%)	Uncertainty (± %)	Normalized (%)
Model 1			
Wishstone best average	49	4	58
Oligoclase BUR-3680 48	5	6	6
Pigeonite	5	3	5
Labradorite WAR-RGAND01 222	4	2	5
Oligoclase WAR-0234 22	4	6	5
Average bronzite	4	2	5
Basalt Glassy Black Flat	4	2	4
Wavellite ML-P7 73	3	1	3
Kieserite KIEDE1 < 1mm	3	1	3
Gypsum var. Alabaster ML-S11	2	1	2
Other (8)	<1		4
Thick dust	7	1	0
Thin dust 2	3	1	0
Slope	15	3	0
Thin dust 1	1	2	0
Blackbody	-7	4	0
Total	101		100
RMS	0.070		
Model 2			
Oligoclase BUR-3680 48	14	3	21
Pigeonite	11	4	17
Labradorite WAR-RGAND01 222	9	3	13
Kieserite KIEDE1 < 1mm	8	2	12
Basalt Glassy Black Flat	7	1	11
Olivine KI 3115 Fo68	3	1	4
Average enstatite	2	2	4
Average bronzite	2	4	3
Anhydrite ML-S9	2	1	3
Meta-variscite ML-P4 95	2	1	3
Glauberite GBYAZ1-R1	2	1	2
Pyromorphite ML-P3 77	1	2	2
Other (6)	<1		5
Thick dust	15	1	0
Thin dust 1	8	3	0
Thin dust 2	3	1	0
Slope	38	3	0
Blackbody	-19	5	0
Total	111		100
RMS	0.119		

Table 4. Keystone Subclass spectral deconvolution results

End-member	Abundance (%)	Uncertainty (± %)	Normalized (%)
Model 1			
Wishstone best average	41	2	64
Quenched Basalt	8	4	12
Kieserite KIEDE1 < 1mm	4	1	7
Basalt Glassy Black Flat	3	2	5
Celestite ML-S13	3	1	4
Pigeonite	2	2	3
Other (8)	<1		4
Thick dust	7	1	0
Thin dust 1	0	0	0
Thin dust 2	0	0	0
Slope	13	2	0
Blackbody	17	3	0
Total	101		100
RMS	0.076		
Model 2			
Kieserite KIEDE1 < 1mm	10	2	19
Basalt Glassy Black Flat	8	2	17
Pigeonite	6	3	12
Bytownite WAR-1384 177	6	9	12
Shocked An 22.6 GPa	5	11	9
Oligoclase BUR-3680 48	5	3	9
Anhydrite ML-S9	2	1	4
Meta-variscite ML-P4 95	2	1	3
Olivine KI 3008 Fo10	1	1	3
Pyromorphite ML-P3 77	1	2	2
Olivine KI 3362 Fo60	1	3	2
Apatite ML-P1 86	1	0	2
Other (4)	<1		5
Thick dust	13	1	0
Thin dust 1	4	2	0
Slope	28	3	0
Blackbody	10	6	0
Total	104		100
RMS	0.130		

941 **Table 5.** Keel Subclass spectral deconvolution results

End-member	Abundance (%)	Uncertainty (± %)	Normalized (%)
Model 1			
Wishstone best average	23	3	35
Bruce	19	5	29
Basalt Glassy Black Flat	5	1	8
Oligoclase BUR-3680 48	4	1	6
Maskelynite (chunk) ASU-7591	2	2	4
Nontronite WAR-5108 granular 203	2	1	4
Andesine WAR-0024 175	2	3	3
Anhydrite ML-S9	1	0	2
Basalt Rind Spot B	1	1	2
Other (11)	<1		7
Thick dust	8	1	0
Thin dust 1	1	1	0
Thin dust 2	0	0	0
Slope	5	2	0
Blackbody	22	2	0
Total	101		100
RMS	0.034		
Model 2			
Basalt Glassy Black Flat	11	3	21
Oligoclase BUR-3680 48	10	6	20
Shocked An 22.6 GPa	8	4	16
Average bronzite	3	2	6
Pigeonite	3	2	5
Anhydrite ML-S9	2	0	5
Kieserite KIEDE1 < 1mm	2	1	4
Fe-smectite SWa-1 solid 207	2	2	4
Basalt Rind Spot B	2	2	4
Olivine KI 3362 Fo60	1	1	3
Illite IMt-2 granular 211	1	4	2
Oligoclase WAR-0234 22	1	7	2
Other (11)	<1		9
Thick dust	12	1	0
Thin dust 1	3	1	0
Thin dust 2	0	1	0
Slope	12	3	0
Blackbody	26	6	0
Total	100		100
RMS	0.060		

944 **Table 6.** Watchtower Subclass spectral deconvolution results

End-member	Abundance (%)	Uncertainty (± %)	Normalized (%)
Model 1			
Wishstone best average	30	5	41
Quenched Basalt	16	5	23
Basalt Glassy Black Flat	5	3	7
K-rich glass	3	3	5
Bruce	3	7	4
Nontronite WAR-5108 granular 203	2	3	3
Anhydrite ML-S9	2	1	3
Pigeonite	2	2	3
Gypsum var. Alabaster ML-S11	2	1	2
Oligoclase BUR-3680 48	1	2	2
Basalt Rind Spot B	1	3	2
Kieserite KIEDE1 < 1mm	1	1	1
Other (5)	3		5
Thick dust	12	1	0
Slope	5	4	0
Blackbody	11	7	0
Total	100		100
RMS	0.085		
Model 2			
Basalt Glassy Black Flat	13	4	21
Quenched Basalt	12	8	19
Oligoclase BUR-3680 48	8	2	13
Saponite ASU-SAP01 granular 194	5	6	9
Pigeonite	5	3	8
Anhydrite ML-S9	4	1	6
Meta-variscite ML-P4 95	3	1	4
Celestite ML-S13	3	2	4
Kieserite KIEDE1 < 1mm	3	2	4
Shocked An 22.6 GPa	2	5	3
Olivine KI 3362 Fo60	2	1	3
Average enstatite	1	1	2
Other (6)	<1		3
Thick dust	16	1	0
Thin dust 1	1	2	0
Slope	12	4	0
Blackbody	11	8	0
Total	102		100
RMS	0.108		

947 **Table 7.** Bruce spectral deconvolution results

End-member	Abundance (%)	Uncertainty (± %)	Normalized (%)
Model 1			
Saponite ASU-SAP01 granular 194	16	6	21
Labradorite WAR-4524 63	8	6	11
Basalt Rind Spot B	7	3	10
Wishstone best average	7	6	9
Pigeonite	5	2	7
Serpentine BUR-1690 51	5	2	7
Average bronzite	4	1	5
Bytownite WAR-1384 177	4	7	5
K-rich glass	4	3	5
Shocked An 37.5 GPa	3	4	4
Oligoclase WAR-0234 22	3	3	4
Gypsum var. Alabaster ML-S11	2	0	3
Olivine KI 3362 Fo60	2	1	3
Anhydrite ML-S9	1	1	2
Crystalline heulandite (zeo)	1	2	2
Other (2)	<1		1
Thick dust	4	1	0
Thin dust 1	3	2	0
Thin dust 2	2	1	0
Blackbody	22	5	0
Total	105		100
RMS	0.089		
Model 2			
Saponite ASU-SAP01 granular 194	17	4	23
Basalt Rind Spot B	8	2	10
Labradorite WAR-4524 63	7	6	10
Pigeonite	6	2	9
Shocked An 37.5 GPa	5	5	6
Average bronzite	4	1	6
Serpentine BUR-1690 51	4	1	5
Oligoclase WAR-0234 22	4	9	5
Bytownite WAR-1384 177	3	9	4
K-rich glass	3	3	3
Gypsum var. Alabaster ML-S11	2	1	3
KI 3362 Fo60	2	1	3
Crystalline heulandite (zeo)	2	2	3
Shocked An 22.6 GPa	2	11	3
Basalt Glassy Black Flat	2	2	3
Anhydrite ML-S9	2	1	2

Other (2)	<1		2
Thick dust	4	1	0
Thin dust 1	3	2	0
Thin dust 2	3	1	0
Blackbody	20	6	0
Total	105		100
RMS	0.090		

Table 8. Mineralogical trends among different rock classes from Mini-TES and MB results

Parameter	Plagioclase (%)	Amorphous Silicate[a] (%)	npOx[b] (%)	Fe^{3+}/Fe_T[b]	MAI[b] (%)
Wishstone	37	9	17 ± 4	0.42 ± 0.09	31
M80	34	11	NA	NA	NA
Keystone	23	26	23 ± 8	0.51 ± 0.11	45
Keel	20	41	25 ± 2	0.65 ± 0.08	50
Watchtower	13	44	55 ± 14	0.88 ± 0.06	88
Bruce	19	25	NA	NA	NA

[a]Sum of all Mini-TES modeled glass and amorphous silicate phases.
[b]Averages of MB results from Morris et al. (2008); see text for descriptions.

This is a preprint, the final version is subject to change, of the American Mineralogist (MSA)
Cite as Authors (Year) Title. American Mineralogist, in press.
(DOI will not work until issue is live.) DOI: http://dx.doi.org/10.2138/am-2017-5618

Figure 1.

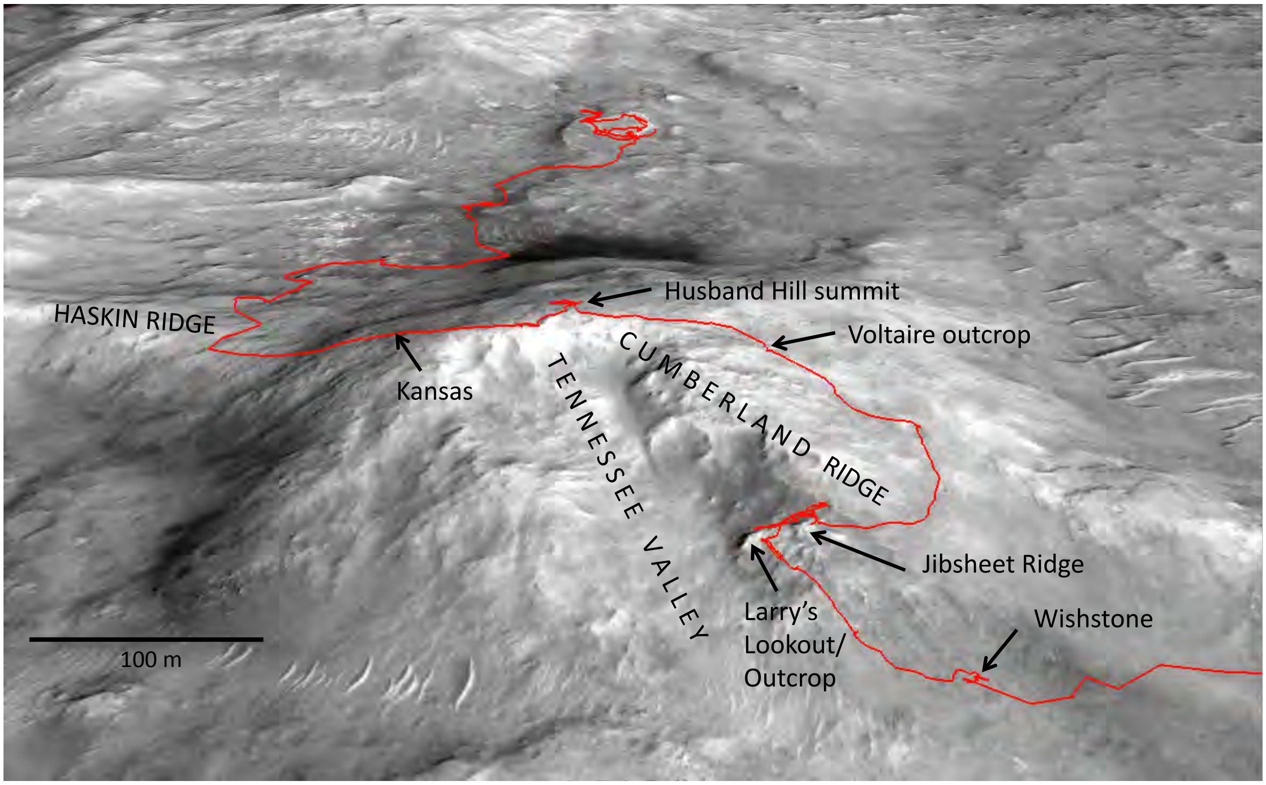

Figure 2.

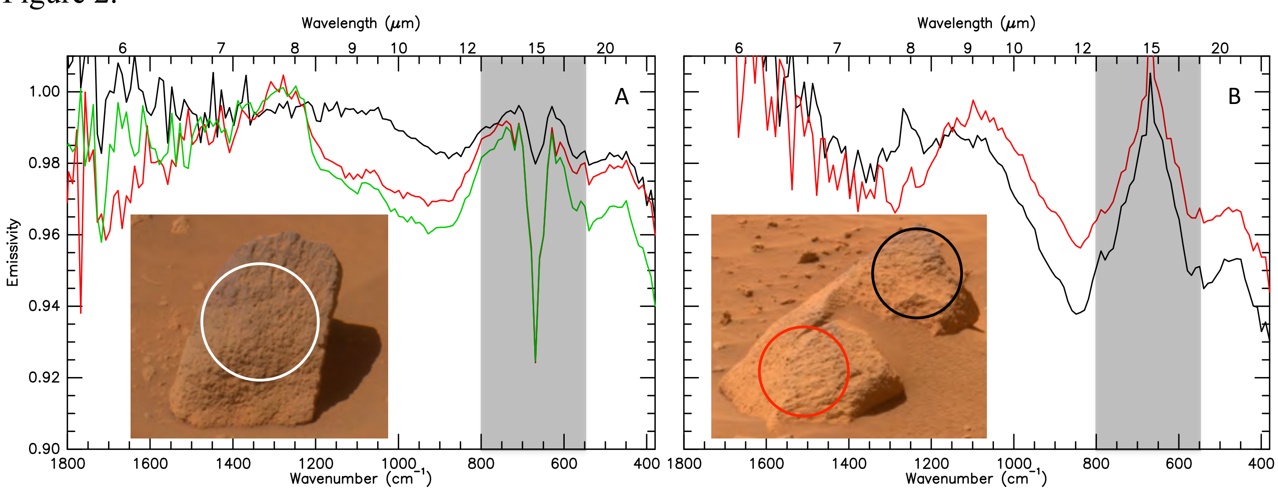

This is a preprint, the final version is subject to change, of the American Mineralogist (MSA)
Cite as Authors (Year) Title. American Mineralogist, in press.
(DOI will not work until issue is live.) DOI: http://dx.doi.org/10.2138/am-2017-5618

Figure 3.

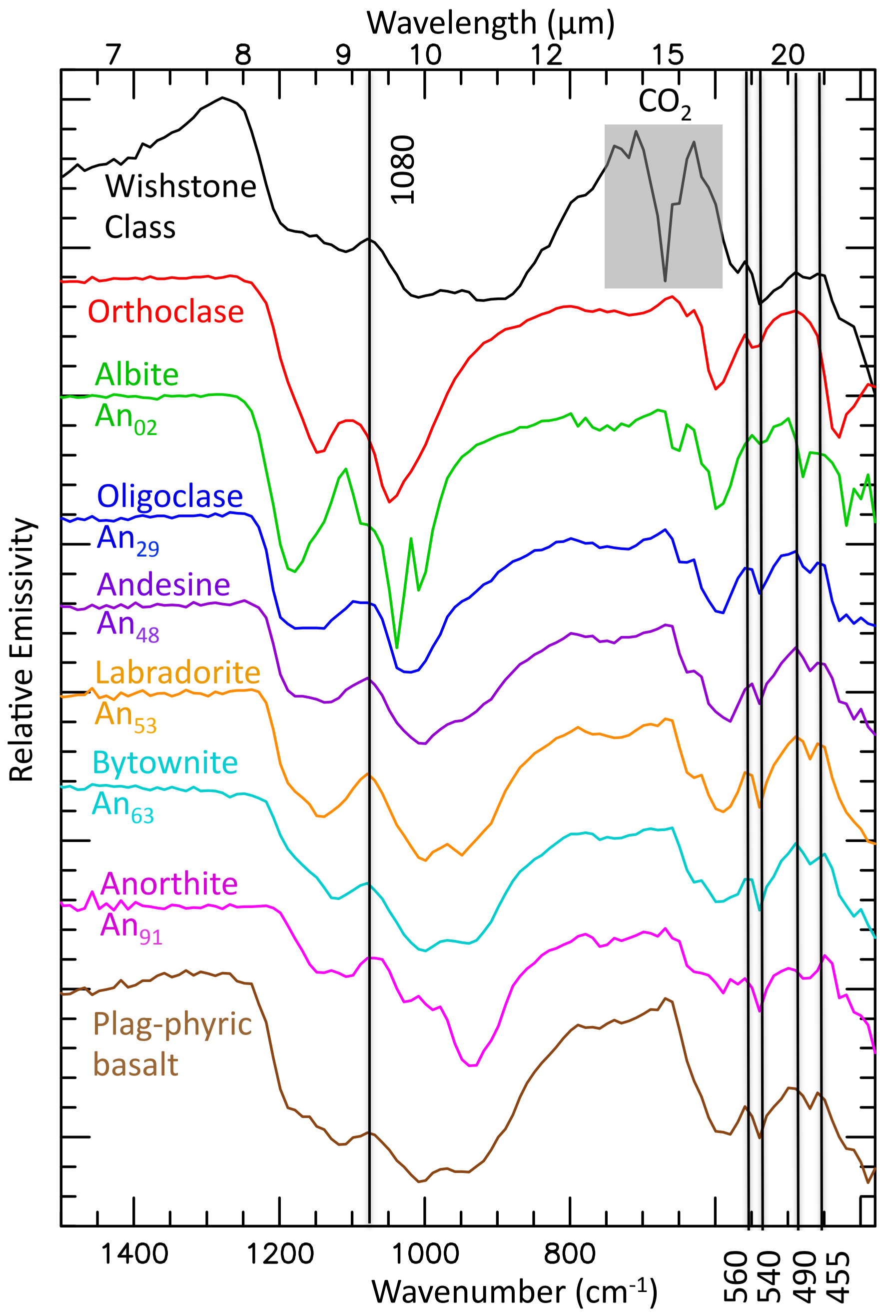

This is a preprint, the final version is subject to change, of the American Mineralogist (MSA)
Cite as Authors (Year) Title. American Mineralogist, in press.
(DOI will not work until issue is live.) DOI: http://dx.doi.org/10.2138/am-2017-5618

Figure 4.

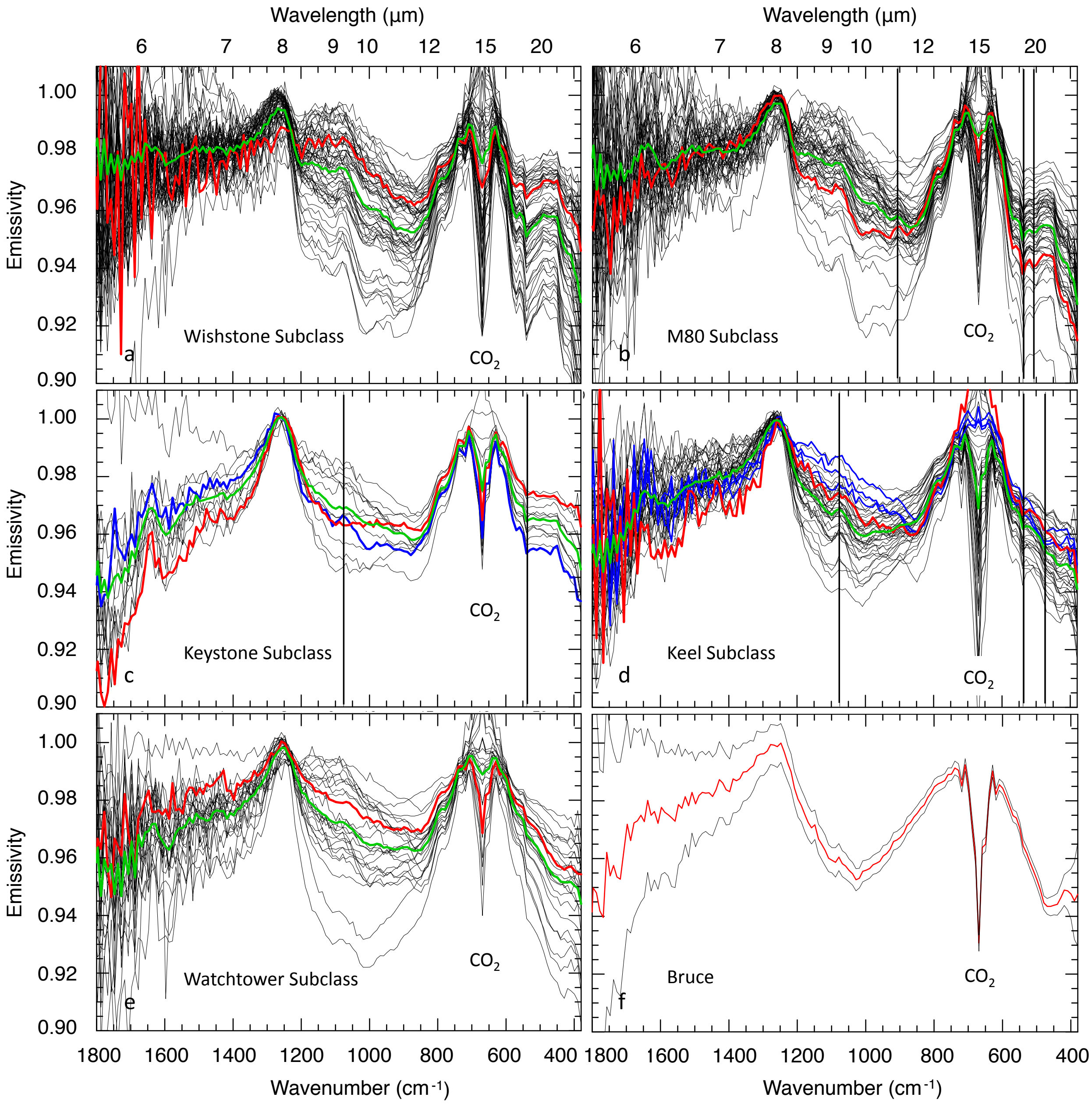

Figure 5.


Wishstone Subclass
Wishstone
sol 342 P2571
Buoy
Sol 506 P2577
Pantheon
Sol 558 P2581
Fraternite
Sol 570 P2538
Rousseau
Sol 561 P2596
Chicory
Sol 647 P2570
M80 Subclass
M80
Sol 531 P2599
Martin
Sol 370 P2537
Bridge
Sol 448 P2545
Garfunkel
Sol 448 P2546
Bolt
Sol 604 P2581
Coreopsis
Sol 647 P2569
Keystone Subclass
Keystone/Madam
Sol 473 P2567
April Fool
Sol 443 P2540
Crone
Sol 465 P2556
Abigail
Sol 468 P2559
Ian Clough
Sol 580 P2546
Ang Rita
Sol 596 P2564
Keel Subclass
Keel
Sol 505 P2553
Foresail
Sol 479 P2578
Fraggle
Sol 492 P2534
Pangboche
Sol 626 P2534
Thyangboche
Sol 629 P2541
Lousewort
Sol 647 P2573
Watchtower Subclass
Watchtower
Sol 419 P2574
Sentinel
Sol 416 P2567
Lamech
Sol 472 P2564
Babel
Sol 493 P2536
Cadge
Sol 492 P2535
Pilot
Sol 498 P2542

This is a preprint, the final version is subject to change, of the American Mineralogist (MSA)
Cite as Authors (Year) Title. American Mineralogist, in press.
(DOI will not work until issue is live.) DOI: http://dx.doi.org/10.2138/am-2017-5618

Figure 6.

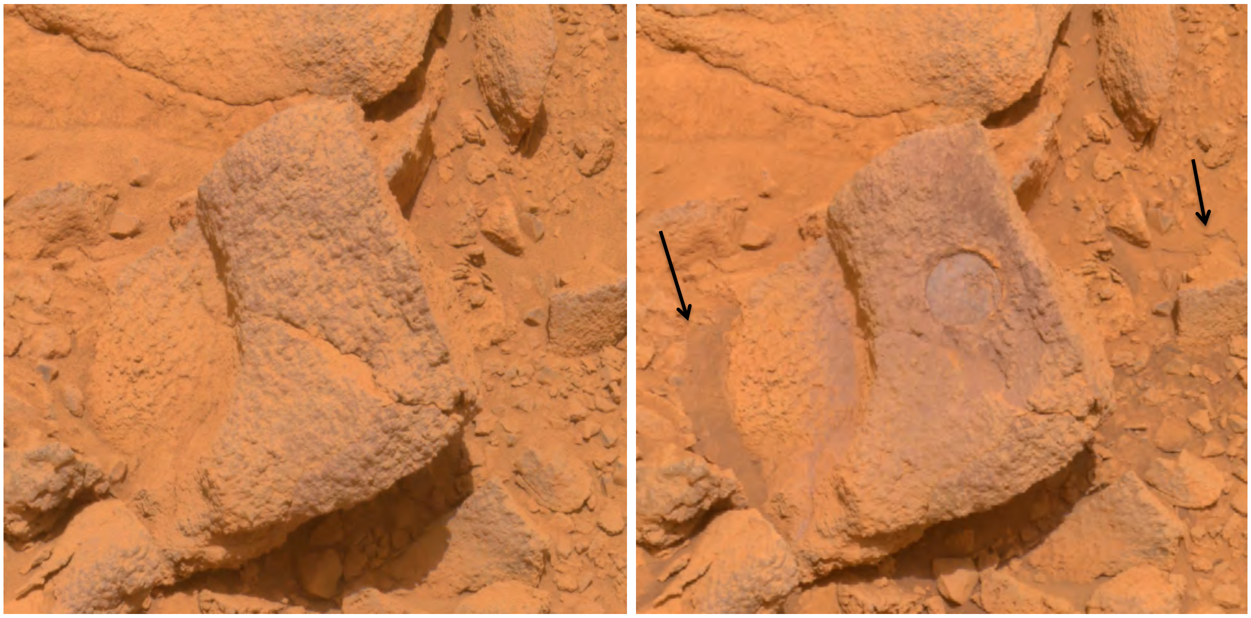

Figure 7.

Figure 8.

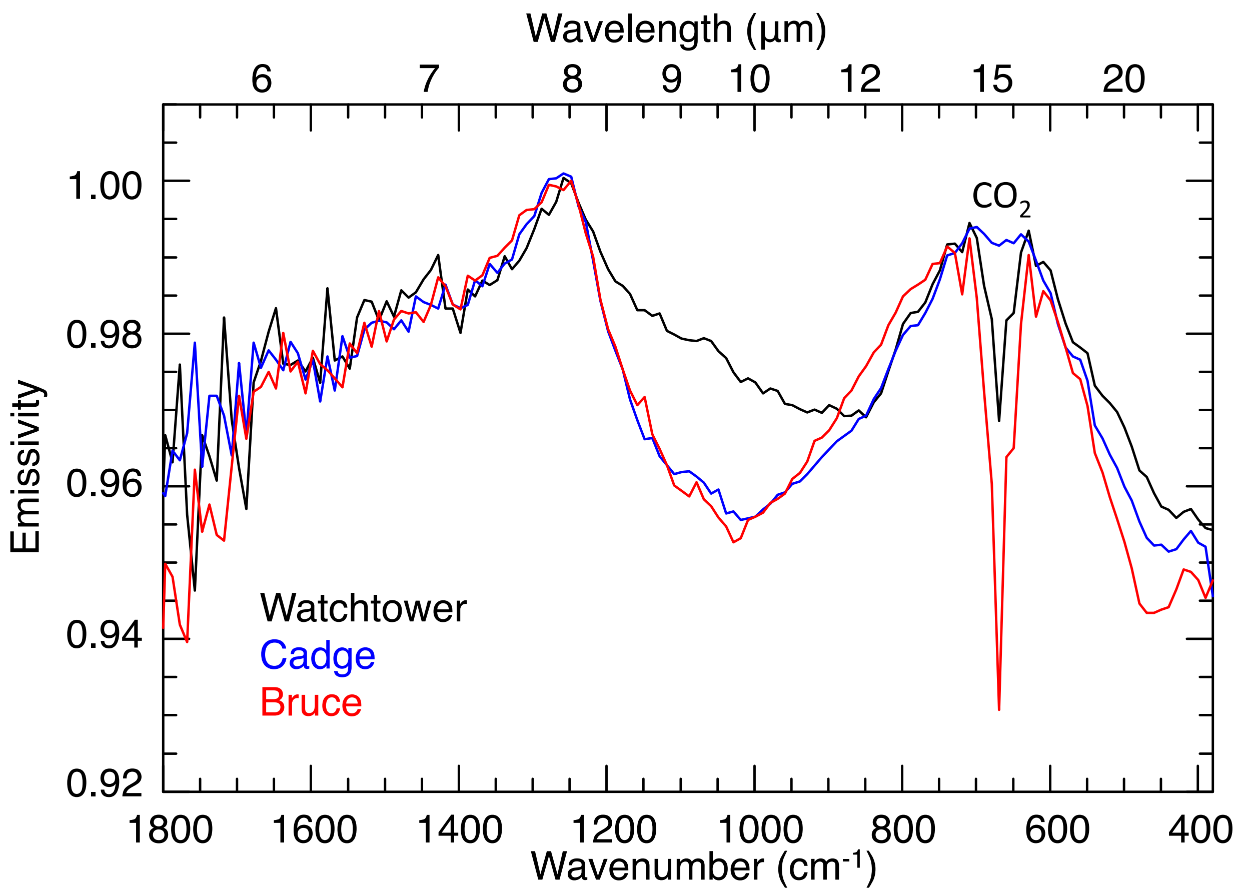
Wavelength (µm)
6
7
8
9
10
12
15
20
1.00
0.98
0.96
0.94
0.92
Emissivity
CO2
Watchtower
Cadge
Bruce
1800
1600
1400
1200
1000
800
600
400
Wavenumber (cm-1)

This is a preprint, the final version is subject to change, of the American Mineralogist (MSA)
Cite as Authors (Year) Title. American Mineralogist, in press.
(DOI will not work until issue is live.) DOI: http://dx.doi.org/10.2138/am-2017-5618

Figure 9.

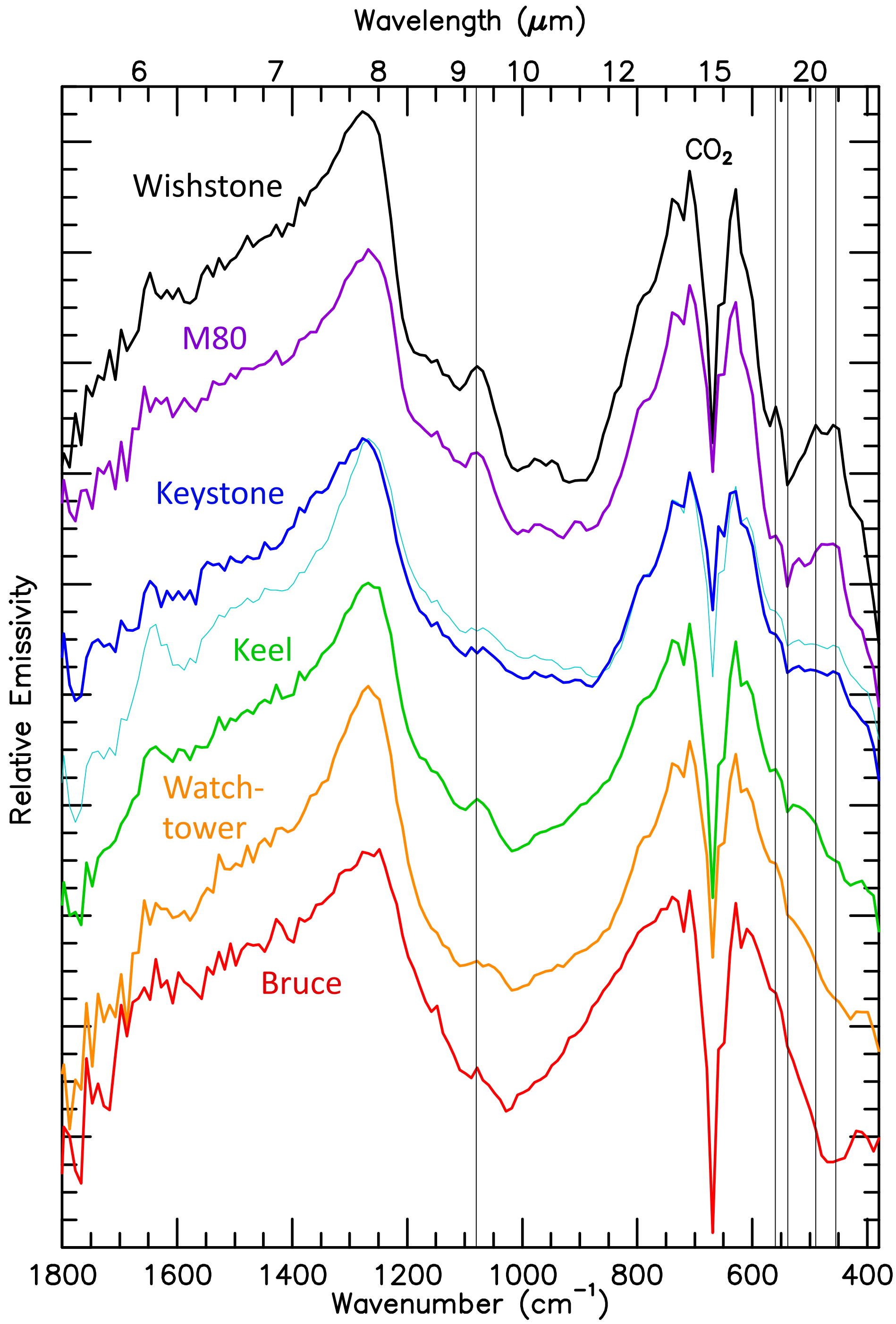

This is a preprint, the final version is subject to change, of the American Mineralogist (MSA)
Cite as Authors (Year) Title. American Mineralogist, in press.
(DOI will not work until issue is live.) DOI: http://dx.doi.org/10.2138/am-2017-5618

Figure 10.

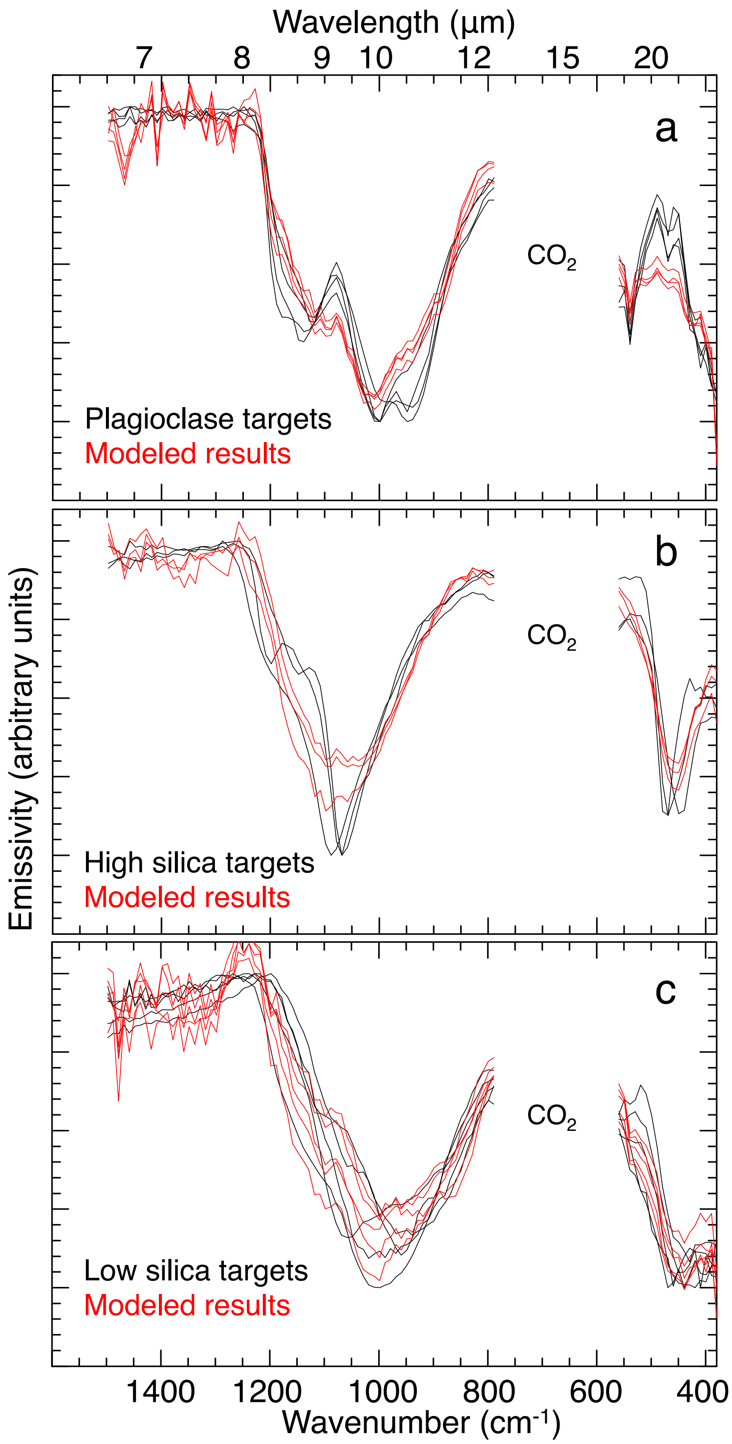

Figure 11.

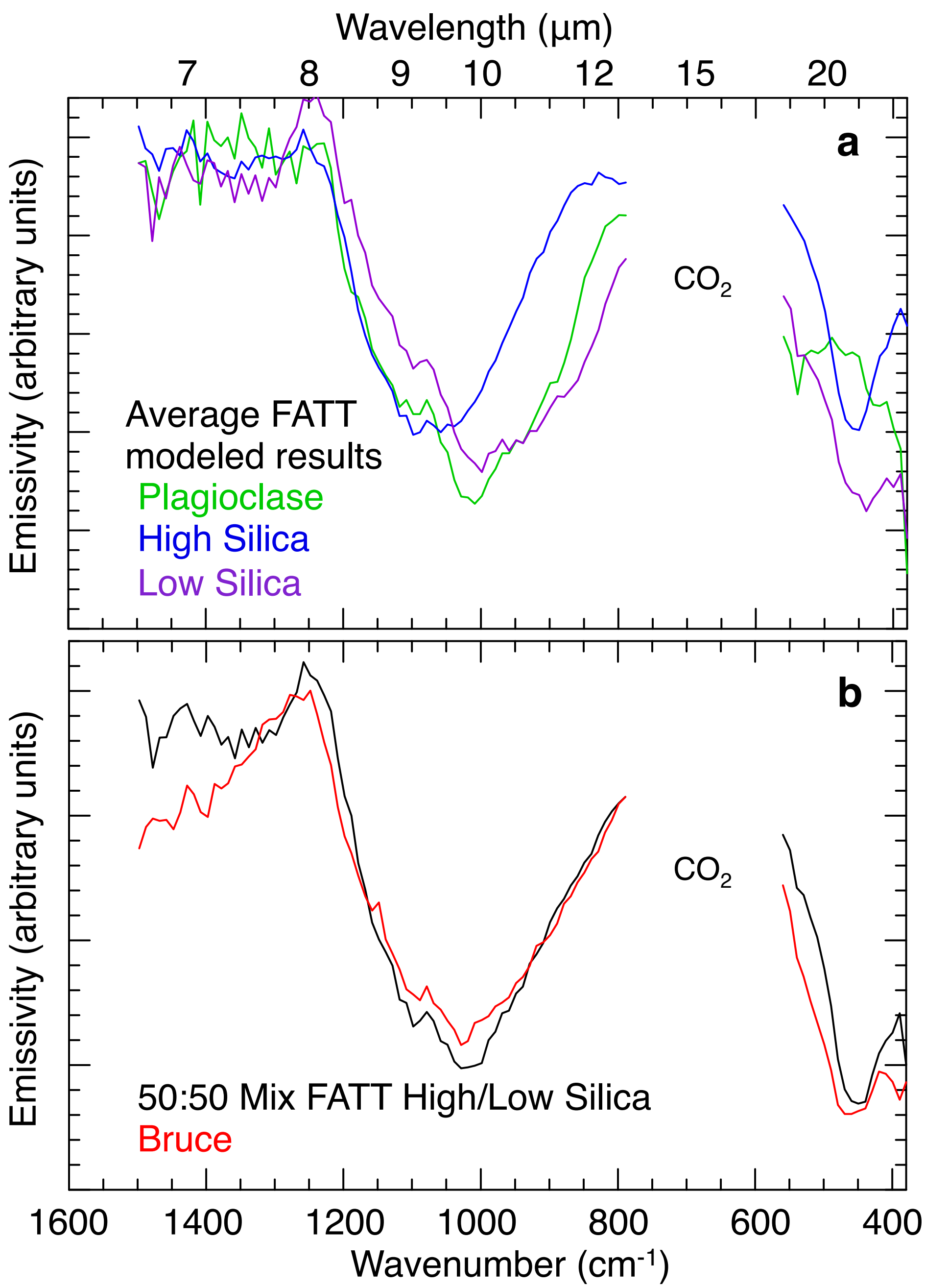
Wavelength (µm)
7
8
9
10
12
15
20
a
Emissivity (arbitrary units)
CO2
Average FATT
modeled results
Plagioclase
High Silica
Low Silica
b
Emissivity (arbitrary units)
CO2
50:50 Mix FATT High/Low Silica
Bruce
1600
1400
1200
1000
800
600
400
Wavenumber (cm-1)

Figure 12.

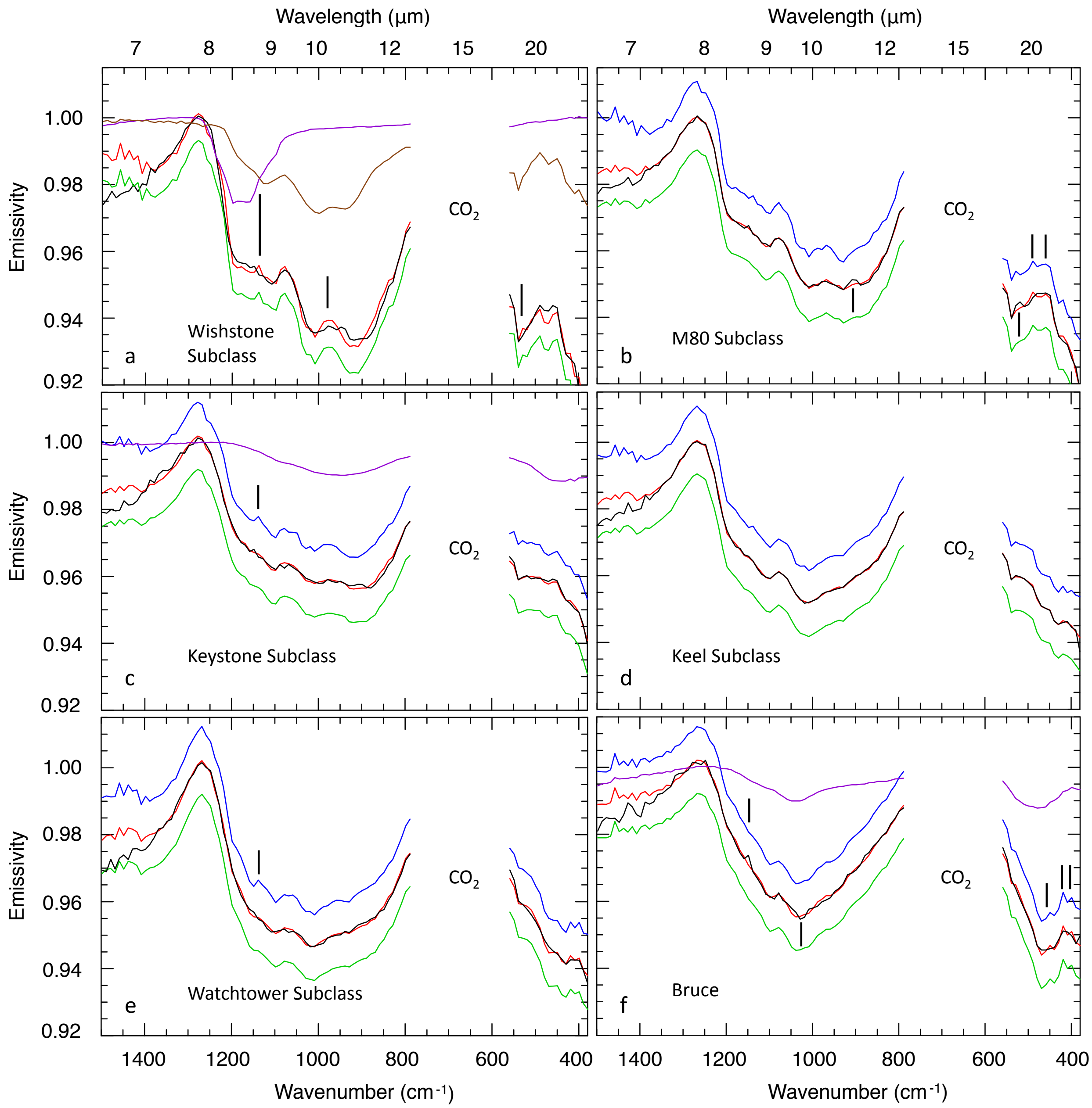
Wavelength (µm)
7 8 9 10 12 15 20
Emissivity
1.00
0.98
0.96
0.94
0.92
CO_2
Wishstone Subclass
a
M80 Subclass
b
Keystone Subclass
c
Keel Subclass
d
Watchtower Subclass
e
Bruce
f
1400 1200 1000 800 600 400
Wavenumber (cm-1)

Figure 13.

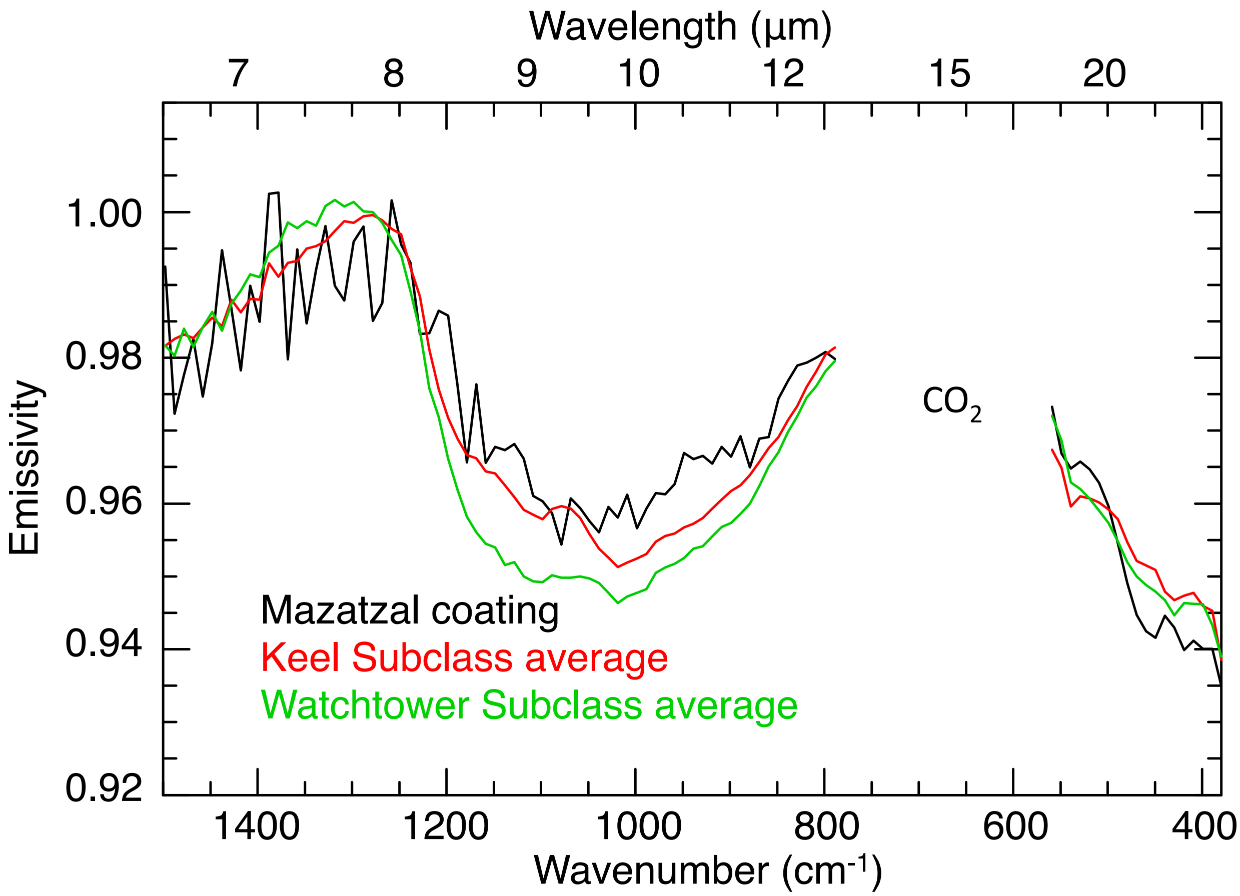
Wavelength (µm)
7
8
9
10
12
15
20
Emissivity
1.00
0.98
0.96
0.94
0.92
CO_2
Mazatzal coating
Keel Subclass average
Watchtower Subclass average
1400
1200
1000
800
600
400
Wavenumber (cm⁻¹)